



ACCESSIBILITY Open

OsloMet – Oslo Metropolitan University

**Department of Civil Engineering & Energy Technology
Section of Civil Engineering**

Master Program in Structural Engineering & Building Technology

MASTER THESIS

TITLE OF REPORT FORMABILITY OF AA5083-H111 ALUMINUM SHEETS FOR USE IN FLOATING PHOTOVOLTAIC STRUCTURES	DATE 15.12.2023
	NUMBER OF PAGES 63
AUTHOR(S) Jon Jibrail	SUPERVISOR(S) Aase Reyes and Sigbjørn Tveit

IN COLLABORATION WITH	CONTACT PERSON
-----------------------	----------------

SUMMARY / SYNOPSIS <p>This investigation focuses on formability aspects of aluminum alloy AA5083-H111 to improve the forming process for floating photovoltaic structures. The study targets the identification of limiting variables and efficiency enhancement. Examining the draw bead distance impact, a safe forming window is established, revealing a significant influence on cup depth within a range of 3 mm to 20 mm. Thickness variations and friction parameters are identified as key contributors to the cup-forming process.</p>

KEYWORDS
Aluminum alloys
Finite element analysis
Deep drawing

MASTER PROJECT ASSIGNMENT FALL 2023

JON JIBRAIL

FORMABILITY OF AA5083-H111 ALUMINUM SHEETS FOR USE IN FLOATING PHOTOVOLTAIC STRUCTURES

Currently, several measures are taken to reduce global warming, where the development of renewable energy sources is one. Solar energy is an essential renewable energy source, and floating photovoltaic (FPV) is growing rapidly. So far, the technology has been developed for use on lakes and other freshwater reservoirs, but now the exploration of using the technology in marine environments have started.

The FPV technology developer Sunlit Sea AS delivers a system of prefabricated floating solar installations designed to handle the chemical and mechanical hazards of the marine environment, where a floating structure made of deep-drawn aluminum sheets are used. The structural geometry must be optimized with respect to several parameters, including heat transfer and material costs, and one constraint is that the sheets must stay intact during the forming operation. Pushing the drawing limit can lead to increased failure rates in the production line, and a better understanding of the influence of certain parameters, e.g. the sheet thickness variation is needed.

Sunlit Sea AS is continually looking to optimize the design of the deep-drawn sheet structure with respect to material reduction, as the material is one of the cost driving factors. The formability is one of the main limiting conditions in this optimization process. In order to develop and optimize the geometry in terms of formability and other factors, Sunlit Sea AS wants to develop a machine learning algorithm that can decide whether a sheet geometry will fail during the deep-drawing process or not. In a first attempt to create a synthetic database for the training of this algorithm, this master project will consider Sunlit Sea's original design, and perform formability analyses to study the influence of certain process parameters.

The project consists of some of the following activities:

1. Theory / literature study / state-of-the-art
2. Development of the numerical formability model in LS-DYNA
3. Parameter study focusing on the forming limits.

The candidate can focus the work on specific parts of the assignment or assess other aspects in consultation with the supervisors.

The form of the report will be as a scientific research report where emphasis is placed on a clear and well-arranged presentation.

Supervisors: Aase Reyes, Oslo Metropolitan University
Sigbjørn Tveit, Oslo Metropolitan University

The report is due at the Department of Built Environment December 15, 2023.

OsloMet, Fall semester 2023

Aase Reyes & Sigbjørn Tveit
Supervisors

Acknowledgements

The author deeply acknowledges and provides deep gratitude to various individuals and collectives whose pivotal contributions were instrumental in the attainment of this thesis. First, the author would like to appreciate the invaluable help from the co-supervisor Sigbjørn Tveit and supervisor professor Aase Reyes, who have generously shared their extensive expertise and experience during the course of this thesis throughout the autumn semester.

The author also wishes to express appreciation for the unwavering support received from friends, family, and the author's employer. Special recognition is extended to Ståle Solberg for accommodating flexibility in the work schedule, which was instrumental in facilitating the completion of this thesis. The flexibility allowed the author to distribute the necessary time and focus for conducting the research effectively.

Lastly, the author expresses heartfelt gratitude to Jina Hanna for her invaluable moral support, and sincere thanks to the Nyquist family for their gracious hospitality.

15.12.2023, Fredrikstad, Norway

Jon Jibrail

Jon Jibrail

Declaration: I, Jon Jibrail, certify that I am the responsible author(s) of this master's thesis. During the preparation of this thesis, the author(s) used Grammarly and other language tools to improve the grammar. The generated content has been reviewed, edited, and verified by the author(s) to ensure accuracy and relevance to the context of the thesis. This disclosure serves to acknowledge the use of Grammarly, and other language tools as described above and to affirm that the authors(s) have taken necessary steps to validate the generated content.

Contents

Acknowledgements	III
Contents	V
List of figures	VII
List of tables	VIII
Notations	IX
1 Introduction	1
1.1 Background and Motivation	1
1.2 Objectives and Scope	5
1.3 Outline	6
2 Theory I	8
2.1 Aluminum Sheets	8
2.2 AA5083-H111	8
2.3 Anisotropy	9
3 Theory II	11
3.1 Plasticity theory	11
3.1.1 Cauchy stress tensor	11
3.1.2 True stress and true strain	12
3.1.3 Voce Hardening Rule	13
3.1.4 Yield functions	15
3.1.5 Lankford constants – R-values	18
3.1.6 Flow-stress ratio, $r\theta$	20
3.2 Material Failure	21
3.2.1 Forming limit diagram (FLD)	21
3.2.2 Marciniak necking – local instability failure	25
3.2.3 Other Factors Influencing Fracture	27
4 Formability Modeling	29
5 LS-DYNA Analysis	33
5.1 Material card 135	33
5.1.1 Weak texture model & Strong texture model	33
5.1.2 Material properties input	34
5.1.3 Two-term Voce rule	35
5.1.4 Yield stress criterion	36

5.1.5 Belytschko-Lin-Tsay formulation	36
5.1.6 Failure criterion	37
5.2 Contact Formulation.....	37
5.3 Parameter Study	38
5.3.1 Mesh Dependencies.....	38
5.3.2 Effects Of Microscopic Sheet Thickness Variations	42
5.3.3 Effects Of Friction	48
5.2.2 Result Matrix	51
6 Summary and Concluding Remarks	57
7 References	60

List of figures

<i>Figure 1: Floating solar panel photo: Sunlit Sea AS</i>	2
<i>Figure 2: Aluminum floating panel</i>	3
<i>Figure 3: Draw bead distance from edge</i>	6
<i>Figure 4: Tensile test of a specimen with θ representing the inclination angle to the rolling direction, denoted as RD [19].</i>	19
<i>Figure 5: Forming Limit Diagram - illustrating the secure forming region from the zone wherein the material exhibits failure [20].</i>	22
<i>Figure 6: Yield locus [23]</i>	24
<i>Figure 7: Forming window for plane stress forming of sheet, [23].</i>	24
<i>Figure 8: Geometric non-homogeneity proposed by Marciniak & Kuczyński, in 1967 [31].</i>	26
<i>Figure 9: Effects of Friction Parameter Variation on Deep Drawing Depth and Wrinkling [32].</i>	27
<i>Figure 10: Blank and tools in LS-DYNA.</i>	30
<i>Figure 11: Forming process of the cup in LS-DYNA</i>	30
<i>Figure 12: Draw bead distance from edge localized in the floating panel.</i>	31
<i>Figure 13: Distance between the cups in the floating panel</i>	31
<i>Figure 14: Velocity and displacement curve, MATLAB.</i>	32
<i>Figure 15: Voce hardening rule curve fit.</i>	35
<i>Figure 16: The blank element, denoting rim nodes in light blue.</i>	39
<i>Figure 17: Force-displacement curves for four meshes.</i>	39
<i>Figure 18: Fracture in the blank.</i>	40
<i>Figure 19: Force-displacement curves for the analyses with Mesh 100 with and without smoothing...</i>	41
<i>Figure 20: Mesh without smoothing.</i>	41
<i>Figure 21: Local necking.</i>	43
<i>Figure 22: Force-Displacement curves from analyses with 3 distinct thickness deviation coefficients.</i>	44
<i>Figure 23: Force-displacement curves for five tests investigating variable outcomes.</i>	45
<i>Figure 24: Thickness distribution throughout the material. Standard deviation set to 0.005 mm.</i>	46
<i>Figure 25: The location of fracture resulting from a randomly distributed shell thickness</i>	47
<i>Figure 26: Region of cup forming and potential failure.</i>	53
<i>Figure 27: Von Mises stress [MPa]</i>	54
<i>Figure 28 Effective Plastic Strain [-].</i>	55

Figure 29: Shell / Blank Thickness [mm]. 56

List of tables

Table 1: Chemical composition of AA5083-H111 9

Table 2: LS-DYNA material model card 135 overview [8]. 34

Table 3: AA5083-H11 material properties. 34

Table 4: Voce hardening rule parameters. 35

Table 5: Yield stress orientation parameters. 36

Table 6: Overview mesh dependency analyses 39

Table 7: Overview of thickness variation analyses..... 43

Table 8: Overview of parameter study due to random thickness distribution 44

Table 9: FEA results investigating friction parameter 49

Table 10: Simulation matrix 53

Notations

<i>AA</i>	<i>Aluminium Alloy</i>
<i>FEM</i>	<i>Finite Element Method</i>
<i>FEA</i>	<i>Finite Element Analysis</i>
<i>BCC</i>	<i>Body-Centered Cubic</i>
<i>FCC</i>	<i>FCC-Centered Cubic</i>
<i>RD</i>	<i>Rolling Direction</i>
<i>TD</i>	<i>Traverse Direction</i>
<i>MK</i>	<i>Marciniak-Kuczynski</i>
<i>WTM</i>	<i>Weak Texture Model</i>
<i>STM</i>	<i>Strong Texture Model</i>
<i>FLD</i>	<i>Forming Limit Diagram</i>
<i>FLC</i>	<i>Forming Limit Curve</i>
<i>DIC</i>	<i>Digital Image Correlation</i>
<i>SD</i>	<i>Standard Deviation</i>
<i>NTNU</i>	<i>Norwegian University of Science and Technology</i>
σ_{ij}	<i>Cauchy stress tensor</i>
$\sigma_1, \sigma_2, \sigma_3$	<i>Cauchy stress tensor principal components</i>
σ_H	<i>Hydrostatic stress tensor</i>
σ_m	<i>Hydrostatic stress</i>
S_{ij}	<i>Deviatoric stress tensor</i>
E	<i>Young's modulus</i>
ν	<i>Poisson's ratio</i>
G	<i>Shear modulus</i>
$\varepsilon_1, \varepsilon_2, \varepsilon_3$	<i>Strain tensor principal component</i>
σ_e	<i>Effective stress</i>
ε_e	<i>Effective strain</i>
Y	<i>Yield stress or flow stress</i>
σ_0	<i>Yield stress or flow stress in reference direction</i>
L	<i>Current length</i>

L_0	<i>Original length</i>
D	<i>Displacement</i>
A	<i>Current area</i>
A_0	<i>Original area</i>
F	<i>Force</i>
e	<i>Nominal strain</i>
s	<i>Nominal stress</i>
ε	<i>Logarithmic strains</i>
σ	<i>Logarithmic (true) stress</i>
T	<i>Thickness</i>
ε^t	<i>Total (logarithmic) strains</i>
ε^p	<i>Plastic (logarithmic) strains</i>
ε^{el}	<i>Elastic (logarithmic) strains</i>
θ	<i>Angle to reference/rolling direction</i>
R_θ	<i>Traverse strain ratio</i>
r_θ	<i>Flow-stress ratio</i>
W_p	<i>Plastic work</i>
M	<i>Non-quadratic yield function exponent</i>
α_i	<i>Yld2000-2d anisotropy coefficients</i>
$X'_{ij} X''_{ij}$	<i>Yld2000-2d linearly transformed stress tensors</i>
α_i	<i>Yld2003 anisotropy coefficients</i>
K	<i>Power/Ludwik's law hardening coefficient</i>
n	<i>Power/Ludwik's law hardening exponent</i>
$\Theta_{Ri} Q_{Ri}$	<i>Voce rule hardening coefficients</i>
$\varepsilon_w, \varepsilon_l, \varepsilon_t$	<i>Strain in width, length, thickness</i>

1 Introduction

1.1 Background and Motivation

In the past century, pollution from human activities primarily from the burning of fossil fuels, has significantly changed the Earth's energy balance [1]. The dominant emission from fossil fuel burning is carbon dioxide. Categorized along with other greenhouse gases, as ozone-depleting substances. These substances contribute to the weakening of the Earth's ozone layer, resulting in temperature increase, commonly recognized as global warming in the media for many years. The noticeable impacts of global warming include the loss of polar ice, melting glaciers leading to rising sea levels and an increase in severe heat waves, causing drought and conditions suitable for wildfires [2]. These observed effects align with predictions made by scientists over years. To reduce the negative effects on the Earth's energy balance, measures must be taken. Currently, renewable energy sources such as solar energy, wind, tides, and geothermal heat are utilized as measures [3]. Solar energy is the radiant energy emitted by the sun, which can be utilized for additional energy production, making it an essential renewable energy source. Notably, the sun stands as one the most rapidly expanding energy source with two primary methods of taking advantage of solar energy: heating or to generate electricity.

This report focuses on solar energy, specifically floating solar panels, shown in *Figure 1*, developed by the project's collaborative partner, Sunlit Sea AS. With a focus on prefabricated manufacturing for expedited production and deployment, to enhance operational efficiency, reduce costs, and enhance overall sustainability. The increasing utilization of floating solar panels has emerged as a concept, aimed to address some of the drawbacks associated with land-based solar installations, such as deforestation and land requirements [4]. These floating panels are positioned in unused lakes, reservoirs, or oceans. Furthermore, the unique advantage of floating solar panels includes their potential to produce more energy than the land-based ones [5]. This increased efficiency is attributed to the cooling effect caused by evaporation on the rear surface of the panels [4].

The good characteristics of aluminum alloys have made it a widely favored material for applications in sheet forming processes and extrusion processes [3]. This is due to its formability characteristics and lightweight properties. An in-depth study of the behavior of aluminum alloys is crucial, as it holds significant effects for optimizing material utilization and mitigating the global environmental footprint

[6]. The significant formability characteristics exhibited by the aluminum alloy(s), under investigation in this study, play a crucial role in shaping the design and production processes of floating solar panels. Developing innovative production methods that enhance material efficiency, resource savings and economical aspects.

There is ongoing research at the Department of Built Environment focusing on fatigue in aluminum and the formability of panels, shown in *Figure 2 a*. The study is specifically narrowed down to examining the formability of the illustrated cup in *Figure 2 b*, fabricated through a deep sheet forming process. This process will be replicated in a finite element analysis program to simulate the actual behavior of the sheet metal. Previous tests conducted by Tveit [7] include material performance tests in various directions to examine anisotropy in the aluminum sheet. Further, analyses are performed in a computing program to explore physical and numerical parameters influencing the formability of the sheet metal.

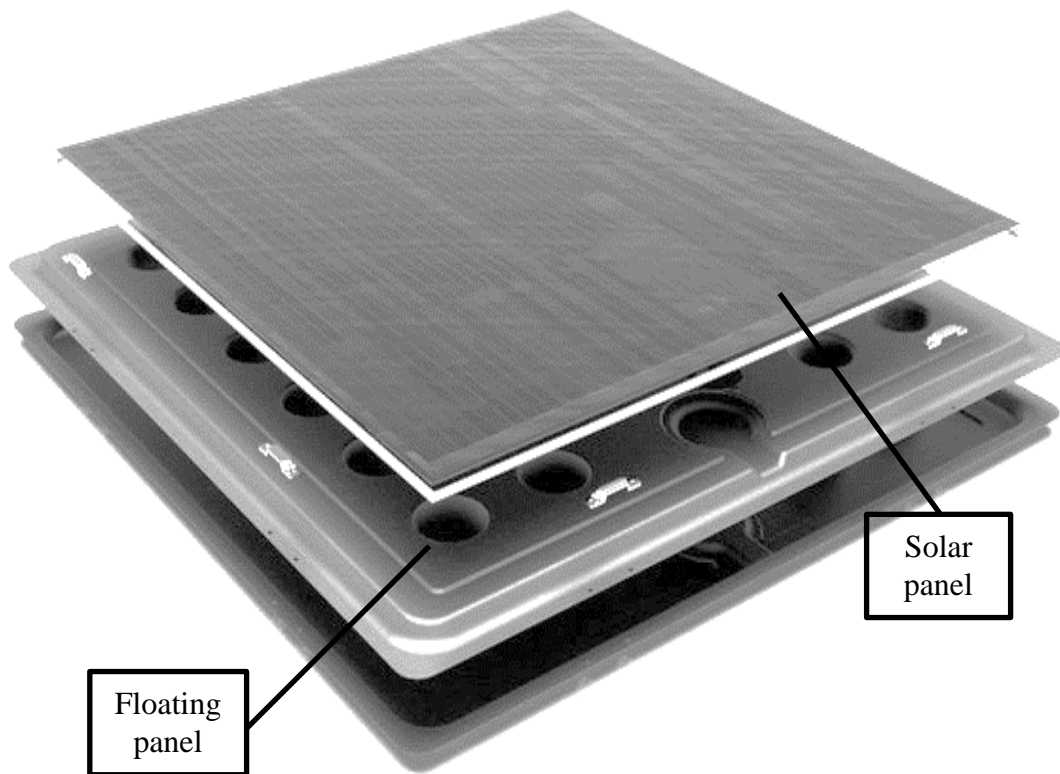


Figure 1: Floating solar panel photo: Sunlit Sea AS

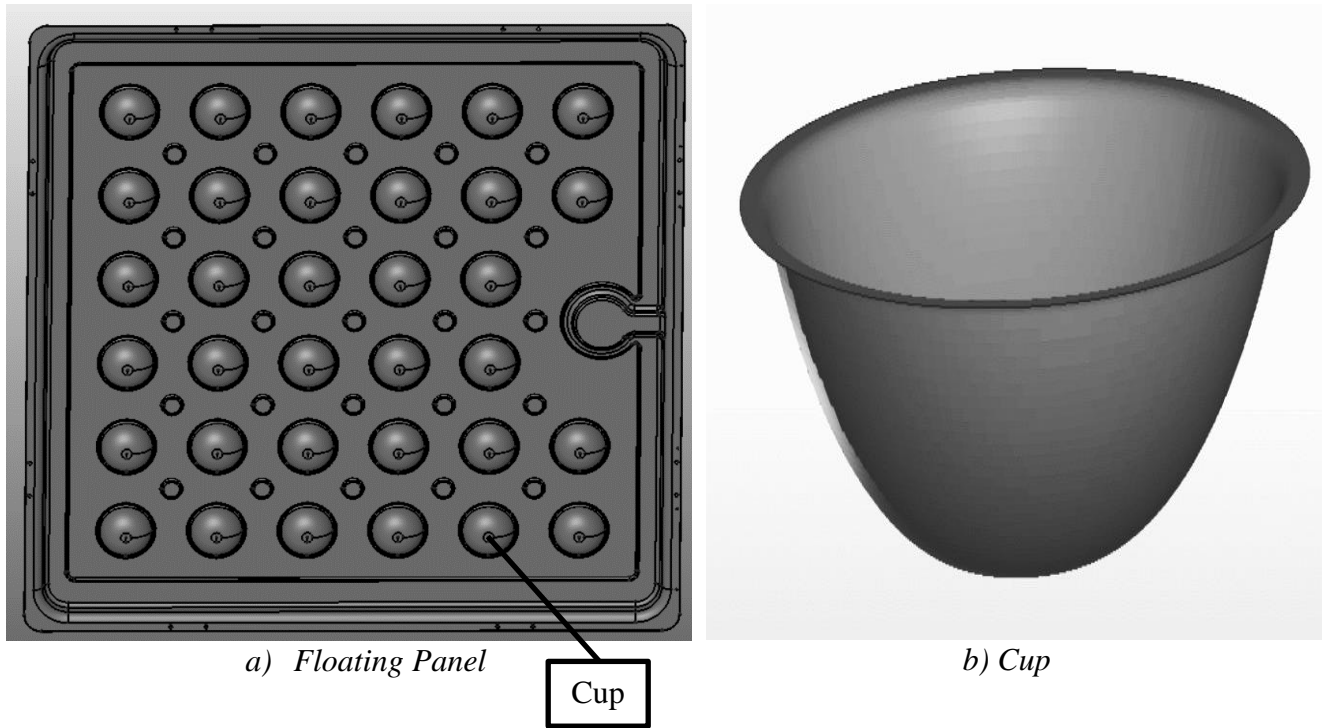


Figure 2: Aluminum floating panel

When investigating sheet metal forming processes for the fabrication of shaped metal sheet products, numerical simulations are performed in a finite element analysis (FEA) program. This is carried out with the purpose of examining the non-linear mechanical responses by these particular aluminum alloy(s). In order to gain understanding of the plasticity and the critical forming inherent in these processes. A precise material model that are initially examined and subsequently integrated into the FEA program to describe limits effectively and precisely. This is done to successfully reconstruct the anisotropic plasticity in the selected aluminum alloy(s) primarily attributed to the rolling process. This aspect has been a central point of comprehensive research over the past years.

Within the framework of this study, a series of analysis have been conducted in the FEA program. Initially, attention is directed towards the behavior of the selected aluminum sheet, a process denoted as parameter study. Subsequently, scientifically validated parameters are identified and applied in further analyses, to address the variables limiting the deep drawing process. The performed analysis is detailed in *Ch.5.3*, covering sensitivity of features such as mesh dependency, thickness variations inherent in the metal sheet, and the various variables initiating fracture. Additionally, a calibration has been conducted

to accurately reconstruct the behavior in experimental data obtained from preliminary work. This calibration ensures alignment with the material hardening curve using the Voce Hardening Rule [8]. Ultimately, the outcomes will be presented in a comprehensive result matrix to identify the relationship between forming limits and parameters related to the deep-drawing process.

1.2 Objectives and Scope

The aim of this report involves conducting deep drawing on a wide range of blank components using a finite element analysis (FEA) program. In the deep drawing process, the blank element, an integral part of the complete aluminum floating panel system, undergoes deformation to take on the shape of a cup. In this thesis, the investigation is limited to the behavior of the cup alone, without its interaction with the overall system. The tests conducted aim to explore diverse material parameter configurations, including variations in geometry. While there was a desire to examine a multitude of geometries as provided by Sunlit Sea, involving variations in several variables to observe cup behavior, this thesis limits its focus to two specific variables: draw depth of the cup and the draw bead distance from the edge. For clarification, the draw bead distance from edge is illustrated in *Figure 3*. Subsequently, a matrix of results will demonstrate the relationship between these two variables. The data presented in the result matrix are focused on these selected variables. Also, a study to gain a deep understanding of the theoretical fundamentals will be presented. This examination will highlight the plasticity theory of metallic materials, anisotropic phenomena, the state-of-the-art of material models, and material failure. Also, earlier experiments conducted by Tveit [7] on the selected material contribute with data regarding the material properties related to its anisotropic behavior. These experimental findings will be incorporated into the FEA program as parameters prior to the computational calculations.

The objective is to develop a parametric design program. A program designed to simplify the input of desired panel geometry with specified parameters. The desired functionality is to assess whether the given panel can be successfully formed or ending up in fracture.

Research Question:

- *How does the variation in draw bead distance from the edge of the aluminum sheet impact material availability for deep drawing, and what role does various physical and numerical parameters play in the formation of deeper cups during the manufacturing process?*

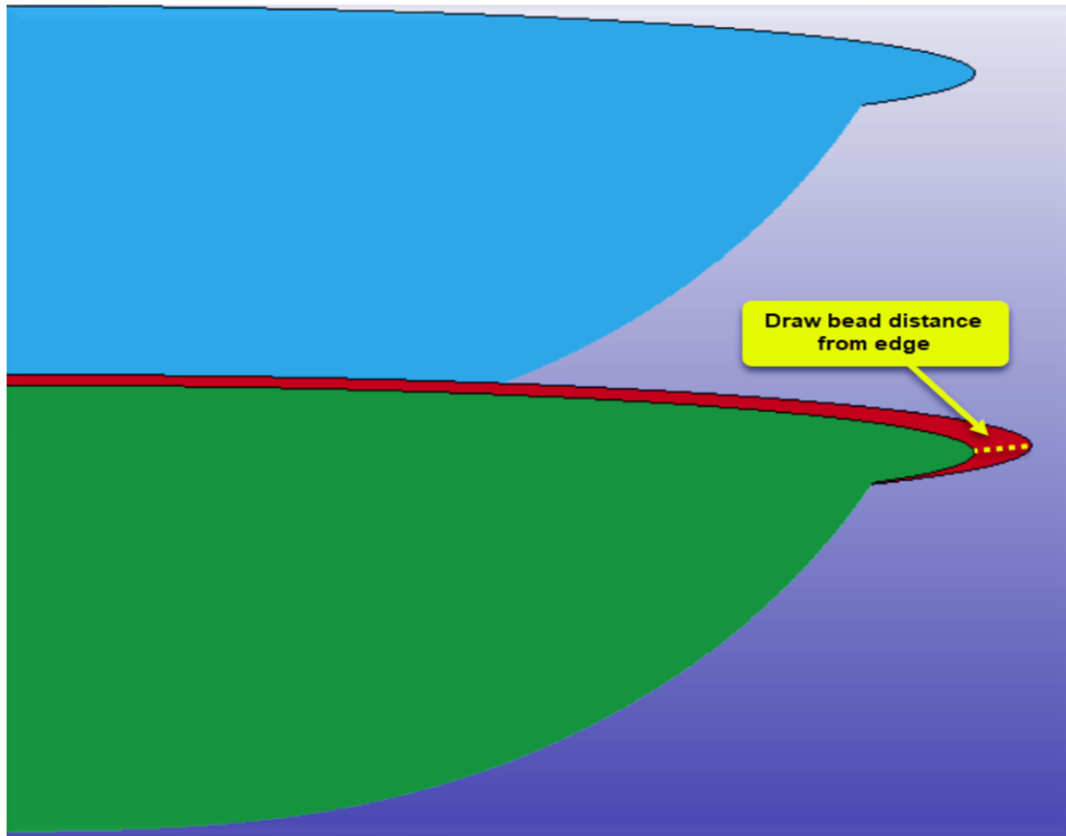


Figure 3: Draw bead distance from edge

1.3 Outline

This chapter outlines the structure of this thesis. *Ch. 2* begins with theory on aluminum, specifically focusing on aluminum sheets and their suitability as a material for floating panels. The first two sub-chapters initially introduce the general theory on aluminum sheets and subsequently introduce the specific properties concerning the chosen aluminum alloy, including its chemical composition. The last sub-chapter addresses the observed phenomena of anisotropy based on tests conducted by Tveit [7], revealing slightly anisotropic behavior. This observation directs the evaluation of a material model to implement in the Finite Element Analysis (FEA) program to accurately describe the material's plastic behavior.

Ch. 3 explores the fundamental theories essential for the formability study: plasticity theory and material failure phenomena. *Ch. 4* outlines the preparations for the finite element sensitivity analyses, presenting

the methodology to achieve the subsequent results. In *Ch. 5*, an advanced yield function, in combination with a fracture criterion, is used to provide a understanding of when the floating panels may experience fractures under varying parameters. Further, a parameter study is conducted. This is studied in the third sub-chapter in *Ch. 5*, where numerous of analyses is performed and presented in a result matrix in the last sub-chapter, along with plots illustrating post-analysis behavior. The findings are continuously discussed throughout the chapter. *Ch. 6* firstly summarizes the conducted work, and secondly reviews the concluding remarks, followed by a sub-chapter suggesting options for further research.

2 Theory I

2.1 Aluminum Sheets

Aluminum formability has been studied for years, and the results are clear, it is one of the most malleable metal, meaning it can be shaped into various forms without risk of breaking [9]. A metal is considered malleable when it can be deformed from its initial shape without development of fracture or splitting. Aluminum has different advantages that makes the material well suited for metal fabrication and shaping. In addition to the material's light weight properties compared to steel, there is numerous of advantages which will be presented further in this chapter.

2.2 AA5083-H111

The selected material for the upcoming investigation is the AA5083-H111 sheet material. The numerical designation '5083' represents the alloy's chemical composition, as provided by the supplier Speira GmbH, and is detailed in *Table 1* for reference. AA5083 is recognized for its exceptional corrosion resistance, high tensile strength, and the malleability, particularly suitable for applications within the marine industry, aligning with the specific needs of this project.

In accordance with standard practices, the temper condition of the aluminum alloy is included in its classification. The temper condition explains the treatments the material undergoes during its production phase and specifies the type of thermal treatment to which it is subjected. In this case, the temper condition 'H111' is employed. Within this designation, the 'H' marks the material as 'strain-hardened,' while the numerical '111' designates a particular variation of this temper condition. This variation involves a systematic annealing process that produces a stable temper state with minimal distortion in the forming process.

Table 1: Chemical composition of AA5083-H111

Al [%]	Si [%]	Fe [%]	Cu [%]	Mn [%]	Mg [%]	Cr [%]	Ni [%]
Base	0.174	0.34	0.058	0.59	4.52	0.069	0.0052
Zn [%]	Ti [%]	B [%]	Be [%]	Ca [%]	Cd [%]	Co [%]	Ga [%]
0.0137	0.0172	0.0002	<0.0001	< 0.0002	< 0.0003	<0.0003	0.0121
Hg [%]	Li [%]	Na [%]	Pb [%]	Sn [%]	Sr [%]	V [%]	Zr [%]
< 0.0005	< 0.0001	< 0.0002	<0.0010	0.0013	< 0.0001	0.0109	0.0011

AA5083-H111 sheets chemical composition, reported by the supplier Speira GmbH.

2.3 Anisotropy

The phenomenon of anisotropy in metals is related to the apparent difference in mechanical attributes in the orientation or direction in which the metal is subjected to measurement. It is important to note that anisotropy can extend to cover certain factors of chemical behavior, however, this report is exclusively focused on the examination of anisotropy in relation to mechanical properties.

Isotropy represent a state in which materials exhibit identical mechanical properties in all measured directions. This state of uniformity is notably challenging to reach in common materials, as directional attributes commonly emerge after various metal processing techniques, including rolling and extruding. Anisotropic behavior is observed in extruded and rolled aluminum profiles. This anisotropy, found within these metallic materials, is characterized by its orthotropic nature, signifying the presence of three distinct mutually perpendicular planes of symmetry at every material point. These planes of symmetry intersect at specific points referred to as the "axes of orthotropy". The introduction of these three axes of orthotropy serves to simplify the mathematical models of elasticity and plasticity. The three mentioned orthotropic axes are in the following order: firstly, along the axis aligned with the rolling direction of the material, the transverse in-plane orientation and the through-thickness direction which is chosen here to be x-, y- and z-axis, respectively.

Aluminum alloys, following the processes of extrusion and rolling, exhibit pronounced textural properties. In the forthcoming sections of the theory chapter, a study will present fundamental plasticity theory and detailing the structure of yield functions.

3 Theory II

3.1 Plasticity theory

3.1.1 Cauchy stress tensor

The Cauchy stress tensor named after the French mathematician Augustin-Louis Cauchy, is a mathematical representation used to describe the distribution of internal stresses in a material at a given point in space and time. States how the normal stress forces and shear forces act on infinitesimal material element. It is characterized by its symmetric second-order stress tensor σ_{ij} as a nine-component in a three-dimensional space, presented as a 3x3 matrix. The i and j represent the cartesian coordinate directions (x, y, z) and the 3x3 matrix is denoted as [10]:

$$\sigma_{ij} = \begin{matrix} \sigma_x & \tau_{xy} & \tau_{xz} \\ \tau_{xy} & \sigma_y & \tau_{yz} \\ \tau_{xz} & \tau_{yz} & \sigma_z \end{matrix} \quad \text{Eq. 1}$$

The normal stresses are noted as σ and shear stress as τ . Upon an examination of the notation above, an inherent symmetry becomes apparent, simplifying the variables by only six individual components.

A shear stress-vanishing frame of reference is a way to rephrase the 3x3 stress tensor matrix, where the shear stresses, which are off-diagonal component of the matrix, are set to be zero. This is achieved through the implementation of a rotational transformation of the coordinate system to establish a principal reference frame. In this reference frame, the stress analysis exclusively focuses on the determination of the normal stresses, denoted as σ_1 , σ_2 , and σ_3 , reducing the complexity of the problem.

Two parts which the stress tensor can be separated to is the hydrostatic stress tensor and the deviatoric stress tensor. The first component is the hydrostatic stress which only acts to change the volume of the material. The second component is the deviatoric stress, which only changes the shape of the analyzed component. The matrix can then be formulated as [11]:

$$\begin{pmatrix} \sigma_x & \tau_{xy} & \tau_{xz} \\ \tau_{xy} & \sigma_y & \tau_{yz} \\ \tau_{xz} & \tau_{yz} & \sigma_z \end{pmatrix} = \begin{pmatrix} \sigma_H & 0 & 0 \\ 0 & \sigma_H & 0 \\ 0 & 0 & \sigma_H \end{pmatrix} + \begin{pmatrix} \sigma_x - \sigma_H & \tau_{xy} & \tau_{xz} \\ \tau_{xy} & \sigma_y - \sigma_H & \tau_{yz} \\ \tau_{xz} & \tau_{yz} & \sigma_z - \sigma_H \end{pmatrix} \quad \text{Eq. 2}$$

Where the hydrostatic stress is given by:

$$\sigma_H = \frac{1}{3} (\sigma_x + \sigma_y + \sigma_z) \quad \text{Eq. 3}$$

3.1.2 True stress and true strain

Stress is a force applied to an area, whereas strain is a change in size. The link between stresses and strains may be defined as true stresses and logarithmic plastic strains, to describe the behavior of a material post yield. To calculate the engineering strain with the help of the post length and the initial length is as follows:

$$e = \frac{L - L_0}{L_0} \quad \text{Eq. 4}$$

The engineering stress is expressed through the utilization of applied force and the initial cross-sectional area:

$$s = \frac{F}{A_0} \quad \text{Eq. 5}$$

The two expressions above, the engineering stress and engineering strain are described as true stress and true plastic strain, respectively expressed as [12]:

$$\varepsilon = \ln\left(\frac{L}{L_0}\right) = \ln(e + 1) \quad \text{Eq. 6}$$

$$\sigma(e, s) = s(1 + e) \quad \text{Eq. 7}$$

3.1.3 Voce Hardening Rule

In a uniaxial tensile testing of for example specimen, the measured stress and strain in the direction of the applied stress can be representative of the effective stress σ_e and effective plastic strain ε_e^p of the material. As a result, such test can provide knowledge of how stress and strain interact in a material during deformation. Power law, the one-term Voce rule, and the two-term Voce rule are mathematical models that describe the behavior of plastic deformations. The formulation of the power law is written on the following form:

$$\sigma_e = K(\varepsilon_e^p)^n \quad \text{Eq. 8}$$

The two-term law that formulates the hardening of a material are the two-term Voce rule, presented in LS-DYNA material model manual [8]. The yield stress, denoted as σ_Y , is defined by a formula consisting of an initial stress and an isotropic hardening expression as represented:

$$\sigma_Y = [\sigma_0 + R(\varepsilon^p)] \quad \text{Eq. 9}$$

The isotropic hardening is expressed as:

$$R(\varepsilon^p) = Q_{R1}[1 - \exp(-C_{R1}\varepsilon_e^p)] + Q_{R2}[1 - \exp(-C_{R2}\varepsilon_e^p)] \quad \text{Eq. 10}$$

3.1.4 Yield functions

3.1.4.1 Von mises yield criterion

The maximum distortion energy hypothesis is another name for the Von Mises yield criteria, named after German American mathematician Richard von Mises [13]. In materials science, the theory is a frequently used yield criterion. The Von Mises yield criterion is also recognized as Von Mises stress or equivalent tensile stress. This criterion is founded on a quadratic isotropic function. The distortion strain energy density of the material determines onset of yield. The stress function is expressed using Cauchy's stress tensor. Prior to reaching yield, the material is assumed to display nonlinear elastic, viscoelastic, or linear elastic behavior. The Von Mises stress is not true stress. It is a value in the theory that compares the uniaxial stress yield limit and the general tridimensional stress. The Von mises stress equation is given by:

$$\sigma_y = \left(\frac{1}{2} [(\sigma_3 - \sigma_1)^2 + (\sigma_2 - \sigma_3)^2 + (\sigma_1 - \sigma_2)^2] \right)^{\frac{1}{2}} \quad \text{Eq. 11}$$

3.1.4.2 Hershey-Hosford

The two anisotropic yield criterion, Yld2000-2d and the Yld2003, are based on the same eight modification components, which, when combined with the plane stress Hershey-Hosford yield function, provide an anisotropic outcome. Yld2003 has a similar setup based on Hershey-Hosford yield function in terms of its components. This higher-order yield criterion effectively bridges the divergence existing between the Von Mises and the maximum shear stress criteria, presented by Hershey in 1954 and later by Hosford in 1972 [14]. Face-centered-cubic (FCC) refers to a specific atomic arrangement, as a cubic lattice, where the face positions are entirely equivalent to each of the eight corners. In 1980 [15] Logan and Hosford proved that yield criterions, when configured with exponent values of 6 and 8, properly models the accurate yield characteristics to sheet metals with body-centered-cubic (BCC) and face-centered-cubic (FCC) crystallographic structures and isotropic mechanical properties. For FCC materials, in this case aluminum, the associated yield function demonstrates great fitness when the yield

function exponent $M=8$ [15]. The generalized isotropic yield criterion, which is presented by W. F. Hosford [14] is presented below.

The Hershey yield function in terms of its principal stresses in plane stress is as follows:

$$|\sigma_1 - \sigma_3|^M + |\sigma_3 - \sigma_2|^M + |\sigma_2 - \sigma_1|^M = 2(\sigma^Y)^M \quad \text{Eq. 12}$$

3.1.4.3 Yield function Yld2000-2d

The yield function Yld2000-2d is a material model used in material research to display the behavior of a material under various loading conditions. This function is designed to study the anisotropic behavior of metallic materials. In particular, materials with anisotropic behavior, which occurs when a material exhibits various characteristics when evaluated in different directions. This yield function relies on eight distinct material constants, consisting of three uniaxial yield stresses, three anisotropic coefficients, a biaxial yield stress, and a biaxial anisotropic coefficient. The high exponent anisotropic yield criteria, ϕ , presented by F. Barlat et al. in 2003 is as follows [16].

$$\phi = \phi' + \phi'' = |X'_1 - X'_2|^M + |2X''_2 + X''_1|^M + |2X''_1 - X''_2|^M = 2(\sigma^Y)^M \quad \text{Eq. 13}$$

This function is achieved through the modification of the principal stress deviators, denoted as s_i , with the introduction of X'_i and X''_i which constitute the principal anisotropic description. This gives a description of the yield stresses of the model and gives a chance for various stresses as input. It is also required to input eight different anisotropy coefficients a_1 to a_8 . These are determined after getting data from eight different stress state experiments. The initial six data points are derived from measurements conducted on specimen tests oriented at 0° , 45° and 90° relative to the rolling direction. Subsequently, the data pertaining to the yield stresses σ_0^Y , σ_{45}^Y and σ_{90}^Y and the Lankford constants, R_0 , R_{45} and R_{90} can be extracted. For a complete description of the anisotropic Yld2000-2d yield criterion, cf. [16].

3.1.4.4 Yield function Yld2003

Taking into consideration the complex mathematics behind the yield criteria Yld2000-2d, Holger Aretz [17] devised and published a new yield criterion in the article "A non-quadratic plane stress yield function for orthotropic sheet metals". When it comes to Aretz's simpler approach, inspired by the Yld89 yield criterion function, the expression for the principal stresses is derived differently. The normal stresses and shear stresses, which is found in the three-dimensional Cartesian coordinates, are simply scaled down to account for material anisotropy and to express how the material's yield behavior can differ with the direction. This allows the anisotropic material to be assigned various stress characteristics in different directions. Consequently, the utilization of the Yld2003 yield function [17] proves to be particularly suitable for effectively characterizing and modeling the anisotropic behavior exhibited by textured materials.

The Hershey yield function in terms of its principal stresses in plane stress is as follows:

$$|\sigma_1|^M + |\sigma_2|^M + |\sigma_1 - \sigma_2|^M = 2(\sigma^Y)^M \quad \text{Eq. 14}$$

Transformations of stresses, Cartesian coordinate system to principal stress frame is:

$$\begin{pmatrix} \sigma_1 \\ \sigma_2 \end{pmatrix} = \frac{\sigma_x + \sigma_y}{2} \pm \sqrt{\left(\frac{\sigma_x - \sigma_y}{2}\right)^2 + \tau_{xy}^2} \quad \text{Eq. 15}$$

The Hershey yield function is divided into two parts to allow for more precise representation of how the anisotropic material behaves. The first part sets the behavior of one set of directions, and the second part sets the behavior along another set of direction.

$$\begin{pmatrix} \sigma'1 \\ \sigma'2 \end{pmatrix} = \frac{\alpha 8 * \sigma_x + \alpha 1 * \sigma_y}{2} \pm \sqrt{\left(\frac{\alpha 2 * \sigma_x - \alpha 3 * \sigma_y}{2}\right)^2 + \alpha 4^2 * \tau_{xy}^2} \quad \text{Eq. 16}$$

The following is the second part of the Hershey yield function, which consists of the three remaining material parameters out of a total of eight parameters, a_5 , a_6 and a_7 :

$$\begin{pmatrix} \sigma''1 \\ \sigma''2 \end{pmatrix} = \frac{\sigma_x + \sigma_y}{2} \pm \sqrt{\left(\frac{\alpha 5 * \sigma_x - \alpha 6 * \sigma_y}{2}\right)^2 + \alpha 7^2 * \tau_{xy}^2} \quad \text{Eq. 17}$$

The simplified yield function Yld2003, with its eight arguments, takes shape as follows:

$$|\sigma'1|^M + |\sigma'2|^M + |\sigma''1 - \sigma''2|^M = 2(\sigma^Y)^M \quad \text{Eq. 18}$$

3.1.5 Lankford constants – R-values

The R-values serve as characteristics of a material's response when subjected to a uniaxial tensile test wherein the specimen is oriented at an angle relative to the rolling direction of the sheet material illustrated in *Figure 4*. The ratio describes the connection between two different components, the gradual plastic strains occurring in the width direction and those happening in the through-thickness direction. To compute the Lankford constant, the connection between the incremental plastic strain in the width and through-thickness direction must be calculated [18]. It is noteworthy that this constant can be accurately described using the strains in these specified directions, as the consistent proportionality in this relationship remains unchanged throughout the analysis. The traverse strain ratio in a given direction in terms of plastic strains can be written as:

$$R_\theta = \frac{d\varepsilon_w}{d\varepsilon_t} = \frac{\varepsilon_w}{\varepsilon_t} \quad \text{Eq. 19}$$

$$\varepsilon_t + \varepsilon_l + \varepsilon_w = 0 \quad \text{Eq. 20}$$

However, for thin metal sheets, as the specimen thickness is small, can be reformulated using Eq. 21. This involves setting the thickness strain equal to the strain in the width and length, resulting in an alternative expression for Eq. 22, and a new traverse strain ratio emerges:

$$\varepsilon_t + \varepsilon_l + \varepsilon_w = 0 \quad \text{Eq. 21}$$

$$R_\theta = \frac{-\varepsilon_w}{\varepsilon_l + \varepsilon_w} \quad \text{Eq. 22}$$

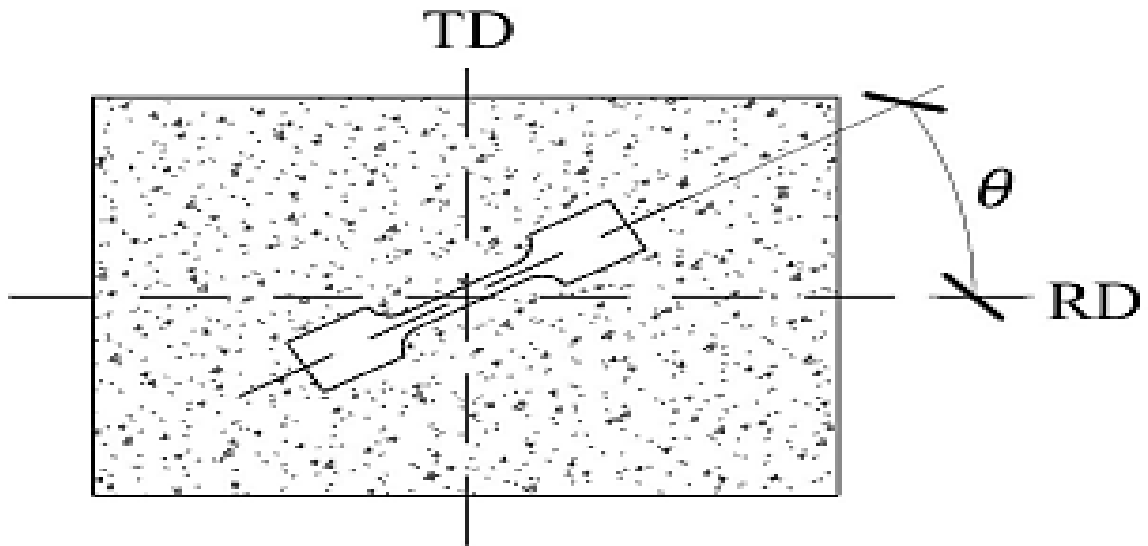


Figure 4: Tensile test of a specimen with θ representing the inclination angle to the rolling direction, denoted as RD [19].

3.1.6 Flow-stress ratio, r_θ

It is crucial to differentiate the flow-stress ratio from the previously mentioned variables, Lankford constants, as these two can sometimes be mentioned together in the literature. The flow-stress ratio serves as a metric for assessing how a material's yield stress varies across different orientations. This aspect holds significance in materials exhibiting anisotropic plasticity behavior, wherein variations in the yield stress become evident in different loading directions. This behavior is quantified by a ratio value denoted as r_θ .

This ratio can be deconstructed into two components: firstly, the flow stress measured in a specified orientation θ relative to the rolling direction, and secondly, the flow stress obtained from another specimen oriented along the rolling direction. Conducting a comparative analysis of the flow stresses is crucial to confirm the validity of the data, given that the coefficient represents a ratio derived from two distinct specimens. The flow-stress ratio is as follows:

Plastic work calculation involves integrating the stress-strain curve over the region where the plastic deformation occurs. Integrating the stress-strain curve gives us an estimate of how much energy is absorbed in the material during plastic deformation. The assessment of plastic work carries significant implications for the calibration of the yield surface. It is observed that considering a broader range of plastic work in the calculation of the flow-stress ratio leads to a notably enhanced accuracy in describing the stress-strain behavior. Plastic work has a lot to say about the calibration of the post-yield curve in the plastic region – taking a range of work in the plastic deformation region will give a much more accurate result of the stress-strain curve [16].

$$r_\theta = \frac{\sigma_\theta}{\sigma_0} \quad \text{Eq. 23}$$

3.2 Material Failure

In this chapter, the theoretical groundwork dictating metal failure is presented, in the context of metal forming processes, aiming to provide an understanding of factors contributing to limitations and potential failure in sheet metal forming-operations.

3.2.1 Forming limit diagram (FLD)

Forming Limit Diagram (FLD) serves as a fundamental tool for describing strain components during deformation from experimental data. Specifically, it represents a graphical representation, positioning major strain ε_1 along the vertical axis and minor strain ε_2 along the horizontal axis. ε_1 expresses the strain resulting from deformation along the principal direction, while ε_2 characterizes the strain occurring from deformation perpendicular to the principal direction [20]. The relation of strains can be calculated directly from Eq. 21 presented in *Ch 3.1.5*.

These axes illustrate the boundary separation regions characterized by strain combinations. Separating between materials undergoing safe plastic deformation from those exhibiting material failure. The region lying beneath the FLD curve (red curve) is acknowledged as the "forming window" illustrated in *Figure 5*. Within this space, material deformation occurs plastically without structural failure.

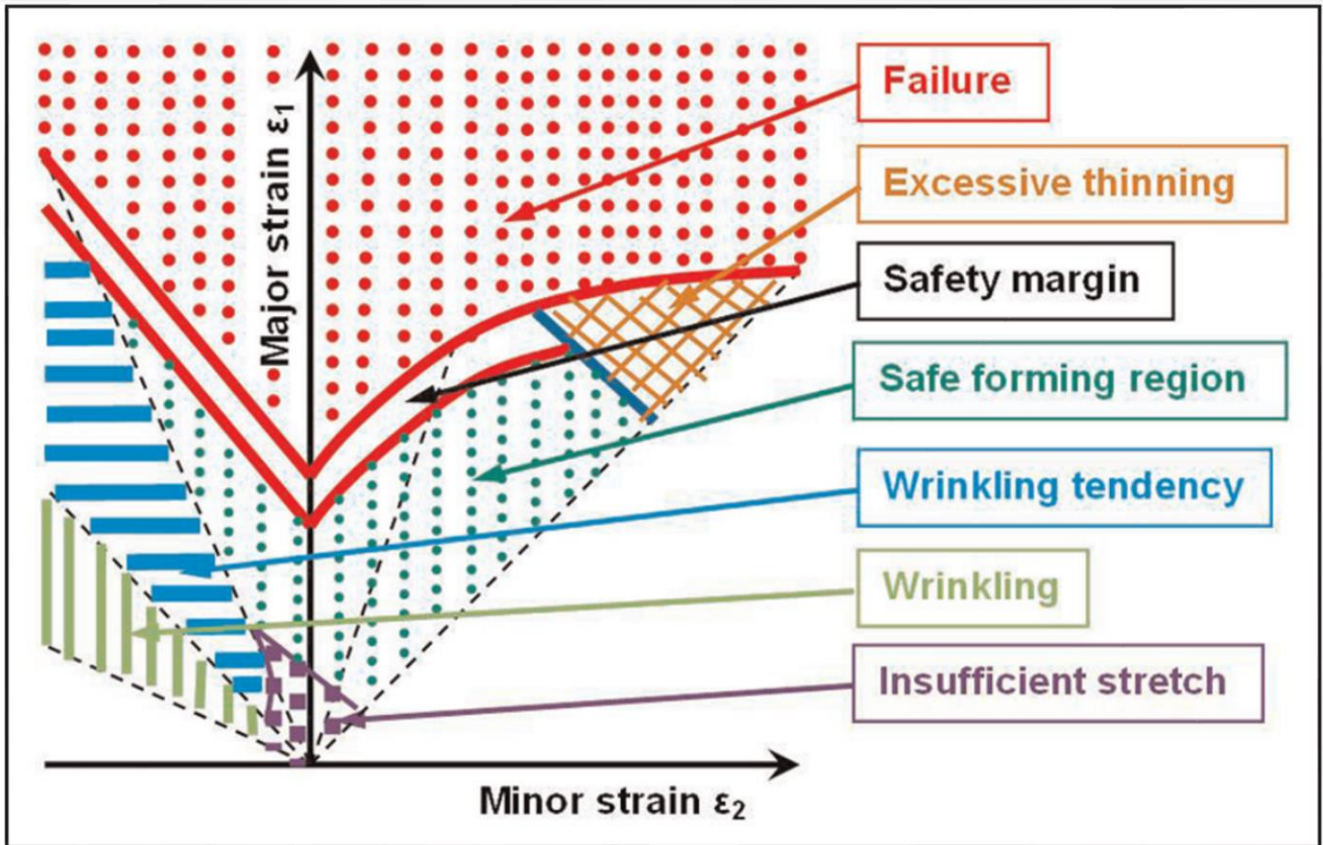


Figure 5: Forming Limit Diagram - illustrating the secure forming region from the zone wherein the material exhibits failure [20].

An introduction of a safety margin, presented by Keeler and Goodwin in 1965-68 [21] [22], achieved through the offsetting of the Forming Limit Curve (FLC) by a margin typically ranging from 10% to 20%. This practice is rooted in the need to account for the natural uncertainties and variations present in the forming process. The rationale behind this safety margin is to address the variations between different FLC's, which assumes linear strain paths, and the real-world complexities where non-linearities often dominate due to complex geometries and loads during forming.

3.2.1.1 Factors effecting the forming window

Strain-hardening index n indicates the height of the FLC drawn from the major strain axis (vertical axis) on the FLD. The FLC intersects the major strain axis at approximately the value of n . Lower value of n , lowers the curve's height, leading to lower formability and smaller area under the curve where plastic deformation can occur in.

Material's anisotropy can affect the forming limit curve because of its different properties in different orientations. Anisotropy is characterized when an R-value is greater than 1. A higher 'R-value' often indicates a material's increased tendency for strong directional dependencies, particularly seen in textured materials. This anisotropy, when coupled with imperfections in the geometry can have influence on the formability. This influence is illustrated by the yield locus distribution in *Figure 6*. A quadratic yield function gives a representation of the yield locus illustrated in *Figure 6 a*, and *Figure 6 b* illustrates a high exponent function. A quadratic yield function extends the yield locus along the biaxial stress axis. This variation directly affects the strain levels observed in biaxial tension analyses. In experimental tests, this behavior is not observed and turns out that a high exponent yield function, with exponents of 6-8, is more realistic for some materials. Changes in the R-value for a high exponent yield function do not have a significant influence on the forming limit curve. [23].

In scenarios requiring the analysis of complex strain paths, an alternative criterion emerges – the Forming Limit Stress Curve (FLSC), presented by Arrieux in 1997 [24]. To clarify, the characteristic of the FLSC is its independence from the specific shape of the strain path, differing from the strain path dependency in the FLD. This attribute makes the FLSC well-suited for the task of predicting necking in situations involving complicated and diverse strain paths.

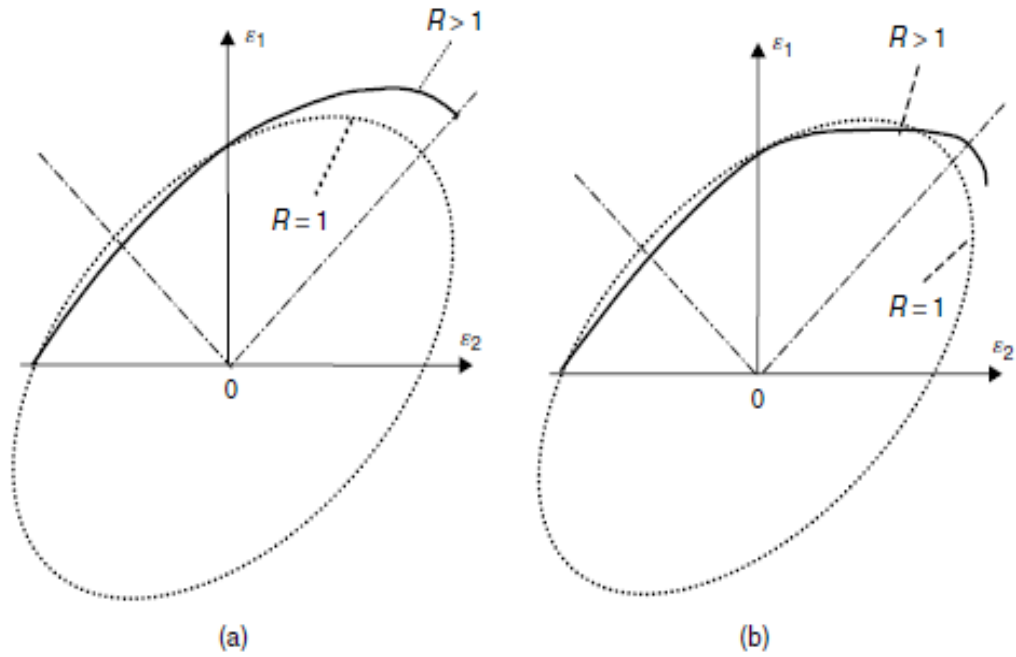


Figure 6: Yield locus [23]

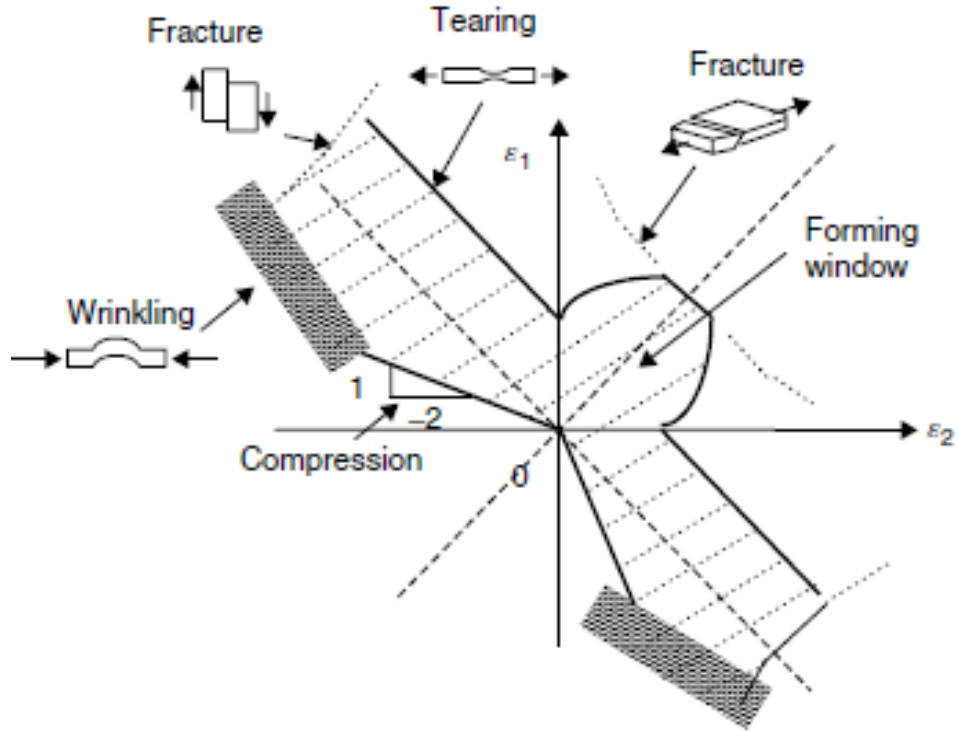


Figure 7: Forming window for plane stress forming of sheet, [23].

3.2.1.2 Wrinkling

In sheet metal forming processes, the occurrence of wrinkling can be attributed to the achievement of critical stress levels in specific regions of the blank. Primarily, the onset of wrinkling in the blank component is dependent upon the geometry of the blank itself and the applied stress conditions. Notably, two primary factors emerge as the principal incentives for the manifestation of wrinkling in sheet metal forming processes, higher yield strengths and reduced thicknesses [25]. Wrinkling analyses can be based on the functional and bifurcation criterion presented by John W. Hutchinson in 1974 in the study of plastic buckling [26]. Wrinkling occurs when ε_{minor} is a negative value, well-illustrated in the forming limit diagram in *Figure 7*. Singh proposed that employing a larger die radius and maintaining a moderate depth could mitigate the probability of wrinkling [27]

3.2.2 Marciniak necking – local instability failure

Marciniak necking is a critical phenomenon that happens during sheet metal forming, characterized by localized thinning, and narrowing of the material during deformation. Marciniak developed a model in 1965 [28] which was formulated from the previous models by Swift [29] (1952) and Tomlenov [30] (1958). This new model was developed to present the grid for limit strains. He introduced that the localization of strains is driven by thickness non-homogeneity in the sheet metal that is going to be formed in the forming process. In 1966, a new model was published in Polish, after some developments done by Marciniak. Later on, in 1967, Marciniak together with Kuczynski published an extended version of the previous model which now is referred to M-K model [31]. In this paper, an addition to the mathematical formulation of the formability model, the paper contained a sensitivity analysis which was rigged for extracting the anisotropic behavior of the chosen material, with parameters such as anisotropy coefficients and hardening exponent and a ratio patterning the thickness non-homogeneity. *Figure 8* shows

two aspects, the geometric non-homogeneity - with section A and B having different thicknesses, and where the localized strains (section B) occur, according to M-K model.

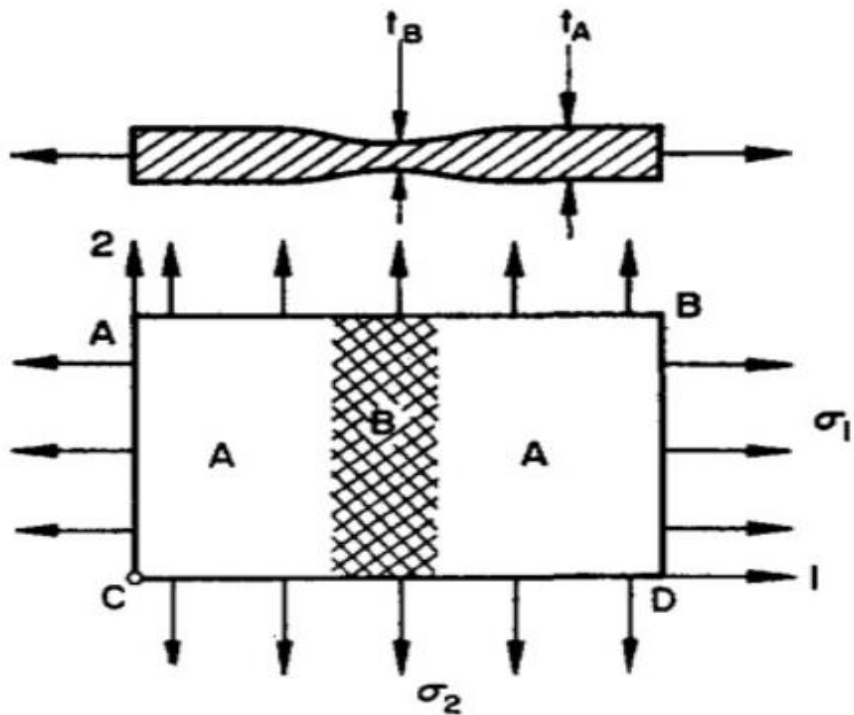


Figure 8: Geometric non-homogeneity proposed by Marciniak & Kuczyński, in 1967 [31].

3.2.3 Other Factors Influencing Fracture

Friction

The friction variable demonstrates a direct proportionality to the extent of damage, exerting a noteworthy influence on damage occurrence [32]. A reduction in the friction parameter corresponds to an increase in forming limits. *Figure 9*, which examines three friction coefficients 0.1, 0.05 and 0.01, illustrates the relationship between deep drawing depth and wrinkling. The friction parameter also increases the normal pressure between the die and blank tool, leading to an elevation in effective stress [33]. According to Pushkar [34], diminishing the friction parameters results in an improved thickness distribution, causing a 9% reduction in thinning when the value is altered from 0.2 to 0.06.

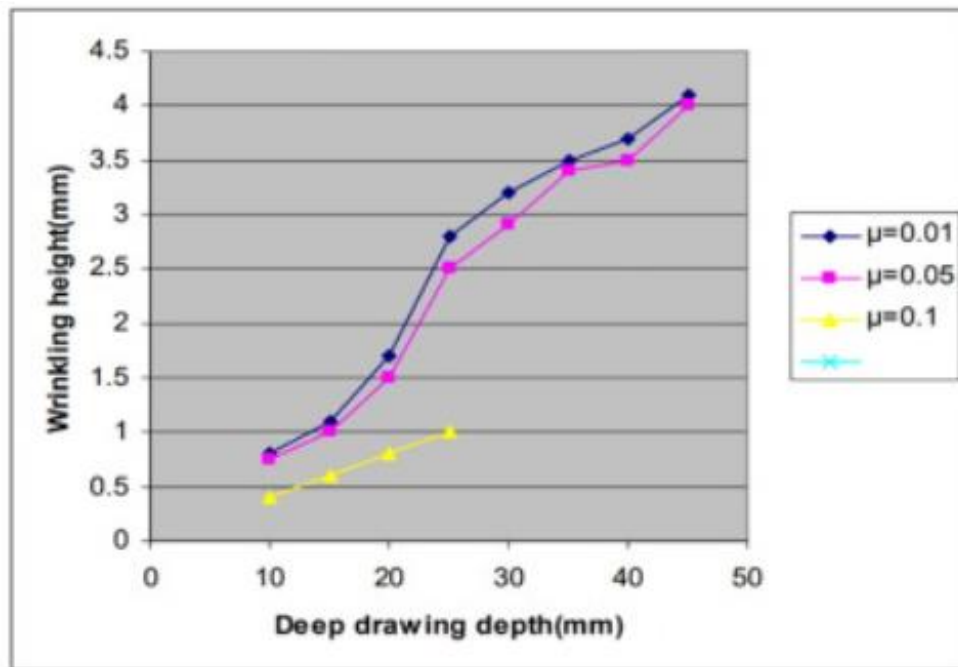


Figure 9: Effects of Friction Parameter Variation on Deep Drawing Depth and Wrinkling [32].

Die shoulder radius

As per Raju [35], the die shoulder radius plays a crucial role in the deep drawing process. A larger radius is associated with an improved ability to draw more material into the cup, thereby reducing the lengthening effect.

Sheet thickness

Reddy's study [36] reveals that an increase in the thickness of the blank sheet influences the effective stress, leading to a heightened cup height and contributing to a decrease in damage. Furthermore, Reddy highlights that thinning is one of the primary contributors to cup damage.

4 Formability Modeling

For a systematic approach, this chapter details the forming process in the FEA program LS-DYNA. This aims to enhance understanding of the deep drawing process before the parameter study. Firstly, *Figure 10* is examined, where the blank element is positioned between punch and die, illustrating a typical deep drawing process. *Figure 11* illustrates the modeled forming process in the FEA program LS-DYNA, aiming to replicate the forming procedures conducted in Sunlit Sea's manufacturing facility. The illustration portrays three components: the punch, controlled by a displacement variable directing its movement in the Z-direction. The blank component with a thickness of 1.51 mm, constrained around the rim, forming a cup that is an intrinsic element of the complete aluminum floating panel illustrated in *Figure 1 Ch. 1.1*. The die part represents the region where the blank sheet undergoes pressing and forming. The model consists of rigid die and punch components. The curve of motion is determined by a MATLAB script involving two adjustable parameters: punch depth and analysis duration. Subsequently, velocity and displacement curves are generated, as illustrated in *Figure 14*. *Figure a* depicts a peak velocity of 60 mm/s within the specified duration. *Figure b* demonstrates a curve of 40mm displacement in the z-direction.

Subsequently, a parameter study is undertaken to investigate influences of various variables on the drawing depth of the cup. The draw depth limit is then analyzed and presented in the result matrix. Two variables will undergo examination: the draw depth in the Z-direction, as depicted in *Figure 10*, and the draw bead distance from the edge of the cup, illustrated in *Figure 10* and *Figure 12* highlighted in red for clarity. Throughout the entire floating panel, there is a uniform distance of 260mm between the centers of the cups and radius of 85 mm, as illustrated in *Figure 13*. An upper limit of 40mm draw bead distance from edge is set. This positioning varies from a distance of zero, where the edge of the blank aligns with the edge of the die and punch, or a wider placement beyond the die and punch components. This investigation seeks to test the hypothesis that an increase in the width hold of the blank element results in increased material availability for deep drawing, consequently enabling the formation of deeper cups. In the result matrix, where the relation between these two variables is presented, a range of displacements spanning from 38.0mm to 42.5mm are tested.

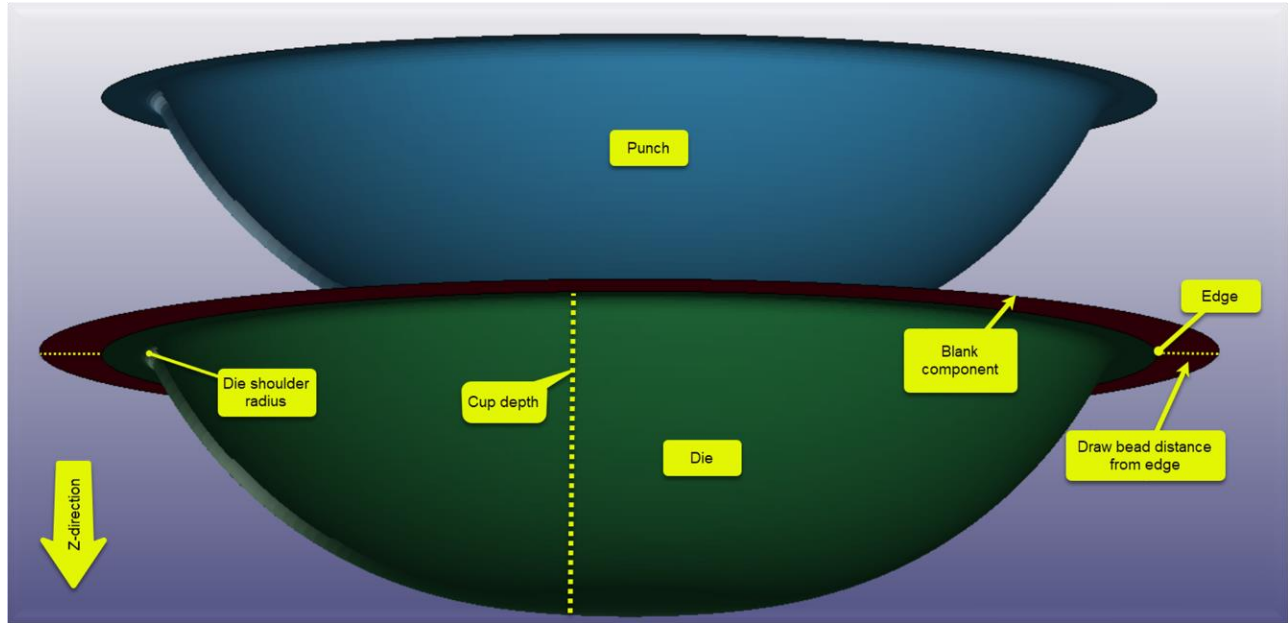


Figure 10: Blank and tools in LS-DYNA.

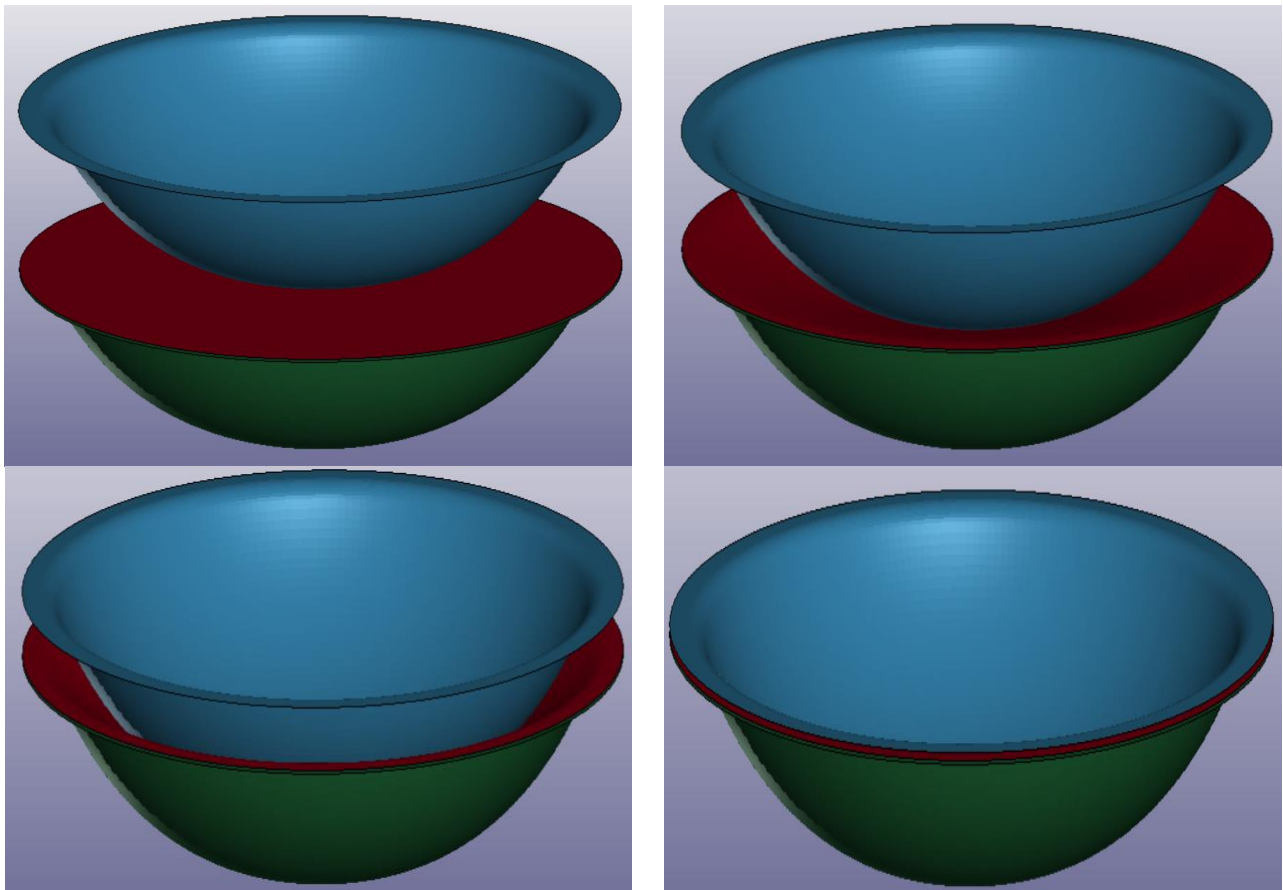


Figure 11: Forming process of the cup in LS-DYNA.

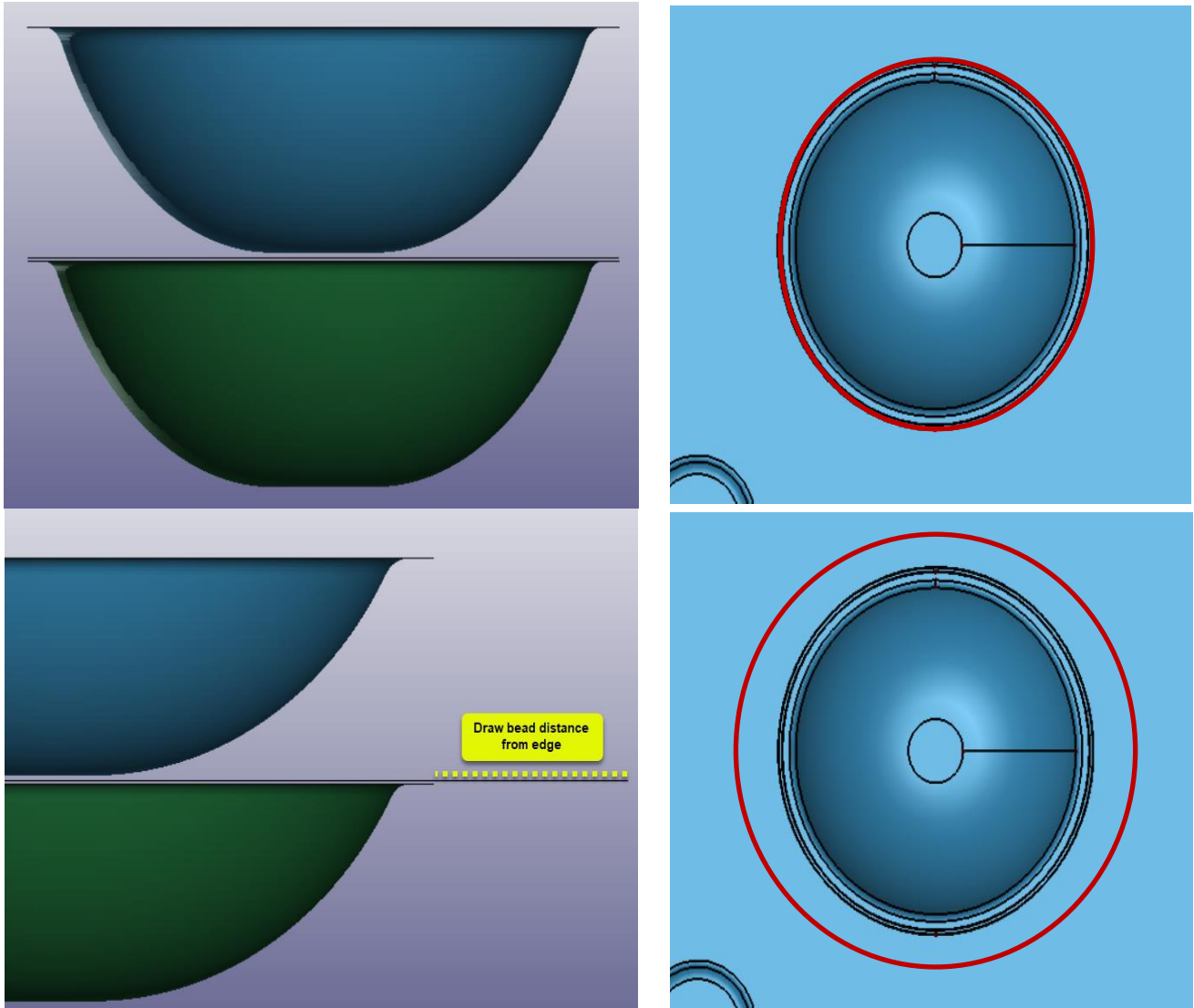


Figure 12: Draw bead distance from edge localized in the floating panel.

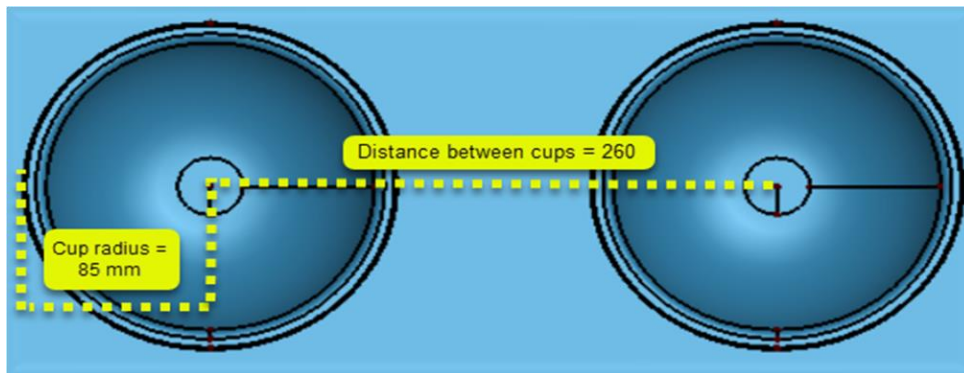
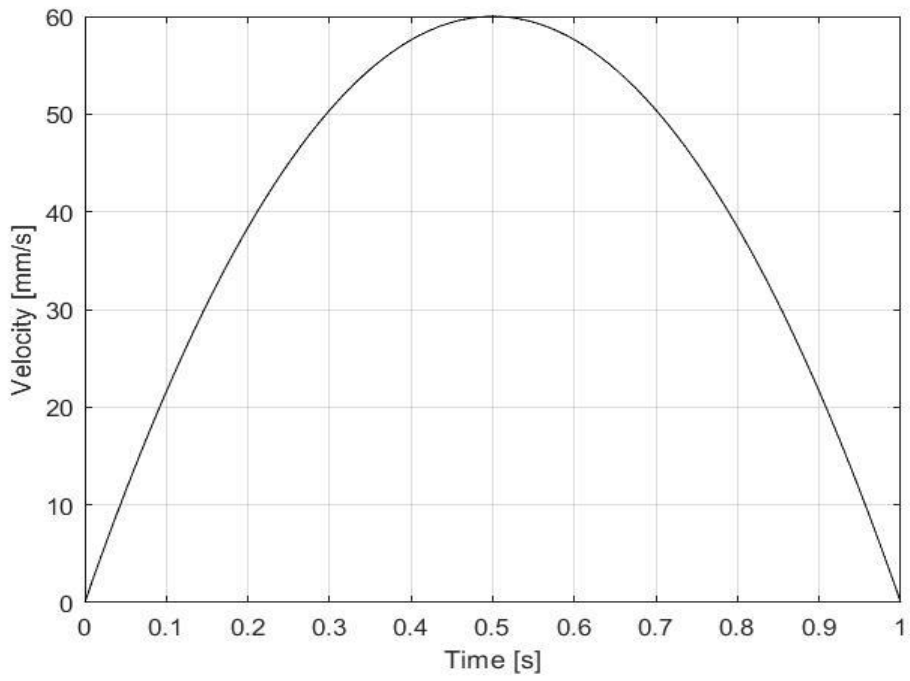
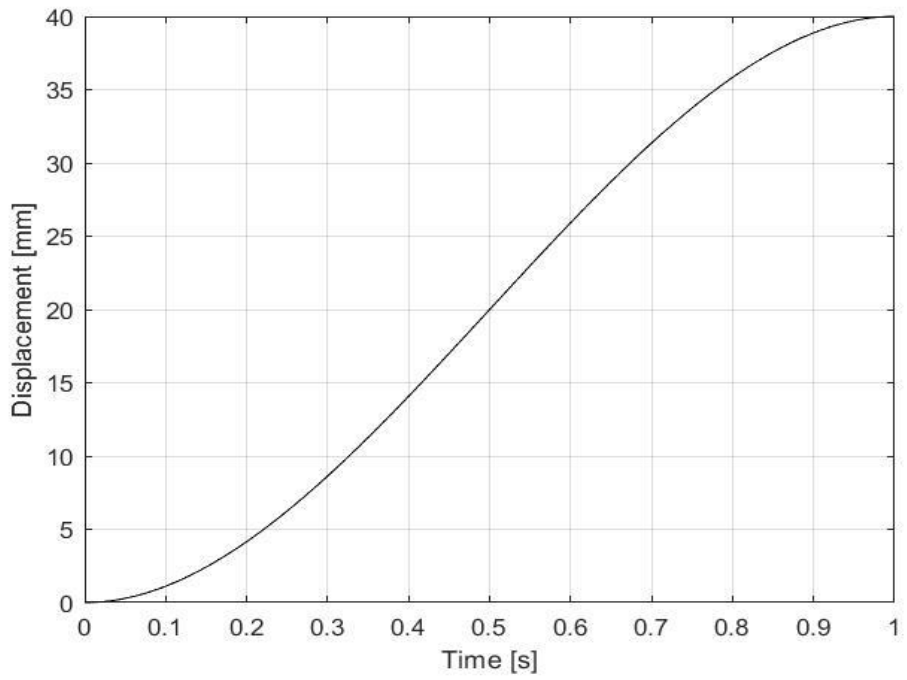


Figure 13: Distance between the cups in the floating panel.



a)



b)

Figure 14: Velocity and displacement curve, MATLAB.

5 LS-DYNA Analysis

5.1 Material card 135

5.1.1 Weak texture model & Strong texture model

In order to accurately characterize the behavior of AA5083-H111, the selection of an appropriate material card is imperative. In this study, Material Card 135 (MAT_135) and the (STM) strong-texture model [17] is chosen in LS-DYNA. With a particular focus on capturing the inherent anisotropic characteristics of the material due to the rolling process. This is an advantage for materials with different levels of anisotropy. This card also includes the ability to include isotropic hardening and kinematic hardening parameters, which is covered in further detail in the LS-DYNA manual [8] and an overview of MAT_135 is presented in *Table 2*.

Material properties (card 1) specifies mass density, young's modulus, Poisson's ratio.

Yield criteria (card 2) is described in this card, either using load curves or as several constants. It also includes four isotropic hardening parameters related to the two-term Voce plastic strain hardening rule. Yield surface parameters (card 3b) describes yield stresses in different directions, assigned here as 0-, 45- and 90-degrees directions. Along with the flow stresses and the R-ratios in the three mentioned directions, the biaxial flow stress and plastic strain ratio is accepted as input for the yield surface calibration.

Kinematic hardening (card 4) includes four kinematic hardening parameters and strain rate parameters. Material axes (card 5,6 & 7) card, where these three cards enable to assign the orientation characteristics of the examined material.

Table 2: LS-DYNA material model card 135 overview [8].

Card 1	Material properties
Card 2	Yield criteria
Card 3a	YLD2003 card
Card 3b	Yield surface card
Card 3c	YLD89 card
Card 4	Kinematic hardening
Card 5, 6 and 7	Orientation characteristics

5.1.2 Material properties input

Aluminum alloy AA5083-H111 material properties reported by the supplier Speira GmbH is presented in *Table 3*.

Table 3: AA5083-H11 material properties.

	Mass density [tonne/mm ³]	Young's modulus [MPa]	Poisson's ratio [-]
LS-DYNA notation	<i>RO</i>	<i>E</i>	<i>PR</i>
	2.650e – 09	7.200e + 04	0.3300

5.1.3 Two-term Voce rule

The Voce curve fitting is conducted within Excel utilizing the Solver add-in, employing a feature designed to minimize the sum product, and later compared with preliminary experimental data as viewed in *Figure 15*. Subsequently, the solved parameters of the Voce hardening rule equations in *Ch.3.1.3*, are gathered and inputted into the material card.

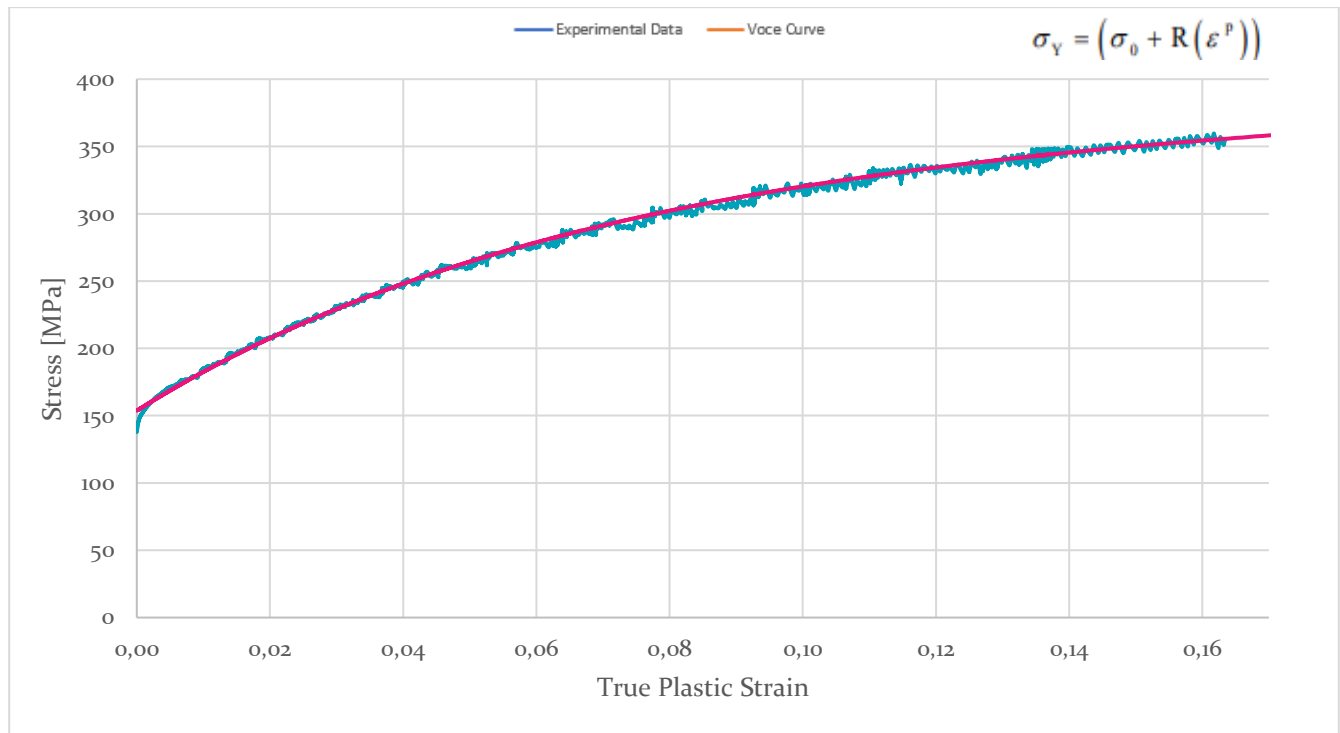


Figure 15: Voce hardening rule curve fit.

The value K is chosen to be half of the yield exponent M which equals to the value 8, $M = 2K$. This is the recommended value in the LS-DYNA manual for FCC materials. The curve fitting values are shown in *Table 4*:

Table 4: Voce hardening rule parameters.

LS-DYNA notation:	$SIGMA0$ [MPa]	$QR1$ [MPa]	$CR1$ [-]	$QR2$ [MPa]	$CR2$ [-]	K [-]
Input:	153.71480	94.32926	2.35239	187.10670	15.35487	4

5.1.4 Yield stress criterion

Yield stresses in different directions are assigned here in 0-, 45- and 90-degrees directions. Along with yield stresses, biaxial flow stress and flow ratio, and R-ratio in the three mentioned directions are defined in *Table 5* [7].

Table 5: Yield stress orientation parameters.

Report notation	r_0 [-]	r_{45} [-]	r_{90} [-]	r_b [-]	R_0 [-]	R_{45} [-]	R_{90} [-]	R_b [-]
LS-DYNA notation	<i>S00</i>	<i>S45</i>	<i>S90</i>	<i>SBB</i>	<i>R00</i>	<i>R45</i>	<i>R90</i>	<i>RBB</i>
	1.000	0.9986	0.9910	1.000	0.6880	0.4250	1.030	0.7850

5.1.5 Belytschko-Lin-Tsay formulation

Belytschko-Lin-Tsay shell element has been implemented in LS-DYNA [37] as an efficient method for performing computationally operations. The mentioned method is an alternative to the Hughes-Lio shell element, described in LS-DYNA theory manual [38].

The Belytschko-Lin-Tsay shell elements with five through thickness integration points requires 725 mathematical operations. This stands in contrast to the under integrated Hughes-Liu element approach which requires 4050 mathematical operations, approximately six 6 more efficient when employing the Belytschko-Lin-Tsay shell elements. Moreover, 35,350 mathematical operations are required for the selectively reduced integration formulation of the explicit Hughes-Liu element. The noticeable efficiency guides confirms the choose of Belytschko shell elements when conducting computational tasks in LS-DYNA. This element formulation is now the default choice for explicit calculations, confirming the approach as a favored option. The chosen Belytschko-Lin-Tsay formulation, referred to as ELFORM 2 in LS-DYNA [39], employs a reduced integration formulation, indicating one integration point in the plane. Five integration points are selected in the through-thickness direction.

5.1.6 Failure criterion

An element erosion criterion, determined by a critical through-thickness plastic strain with a specified limit of -0.5, was employed in the analysis. This criterion should be satisfied in at least three out of the five through-thickness integration points in order for element erosion to occur. Based on preliminary test simulations, the critical value of plastic through-thickness strain was selected such that local necking occurs prior to reaching the limit.

5.2 Contact Formulation

In metal forming processes, the assignment of friction between the blank and the tools is a crucial parameter for achieving acceptable material flow and high-quality surface outcomes. In LS-DYNA, various contact types are available depending on the scenario. The selected contact type for the analysis is one way surface to surface, denoted in LS-DYNA as:

CONTACT_FORMING_ONE_WAY_SURFACE_TO_SURFACE

Within this contact formulation, the assignment of specific values for static and dynamic frictions is enabled. The selected static friction parameter is set at 0.06, while the dynamic friction parameter is set at 0.03.

5.3 Parameter Study

5.3.1 Mesh Dependencies

Mesh dependency related to element failure necessitates the implementation of a non-local formulation wherein neighboring elements' failure/damage variables are averaged. Hence, a parameter study is conducted to discern whether there exists mesh dependency.

Four fracture analyses were conducted to investigate potential mesh dependency in the results, with the only variable subject to modification being the mesh density. A clear fracture is illustrated in *Figure 18*. This analysis aimed to detect whether variations in mesh density influence the onset of fracture, specifically characterized by the number of nodes surrounding the blank element, as illustrated in *Figure 16*. *Figure 17* illustrates the four conducted tests, with values: 150, 200, 296 and 416 representing mesh density. Following the execution of mesh analyses illustrated in *Figure 17*, it becomes apparent that the mesh dependency within the sensitivity analyses is minor. The different mesh densities did not have large impact on the results along the whole motion, the only small difference was at almost full displacement when the model ended in fracture in different time. The selected mesh density for subsequent analyses is set at 200, aligning with a configuration of 200 nodes surrounding the constrained rim of the blank aluminum sheet. Also, employing shell elements with a size of approximately 1.20mm, equivalent to a mesh density of 200, aligns with the studies conducted by SINTEF [40] [41]. Studying this behavior of minimal mesh dependency, it can be argued for, that it is not in need to implement non-local criterion: where the neighboring elements' stress is averaged. Rather, we adhere to the use of the local criterion. Also, it is visualized in *Figure 17* that for the four mesh analyses the results for the two rough meshed models the distance between the graphs where they experience fracture is larger, then the two finer mesh of 300 and 400, where the distance is smaller and somehow converges. This conclude that the error minimizes, and an acceptable behavior is somehow on the way to be reached at a displacement on 41mm. The three rough meshes had greater distance between the fracture equaling 0.05mm in displacement, but for the finest mesh, this distance became smaller which means the distance between the 296 and 400 mesh at fracture is now 0.03, a slight difference, but in the right way.

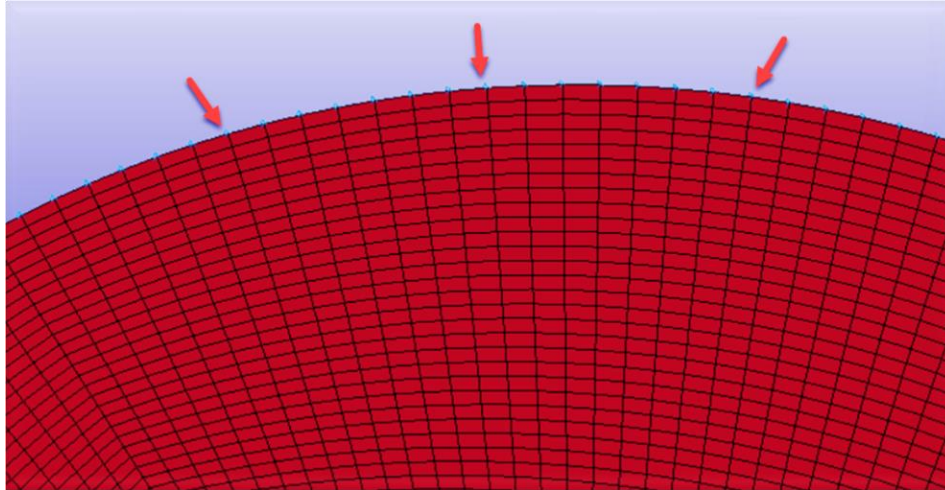


Figure 16: The blank element, denoting rim nodes in light blue.

Table 6: Overview mesh dependency analyses

	Mesh dependency
Shell thickness [mm]	1.51
Mesh density	150, 200, 296, 416
Number of tests	4
Z-displacement after completing movement [mm]	44.0

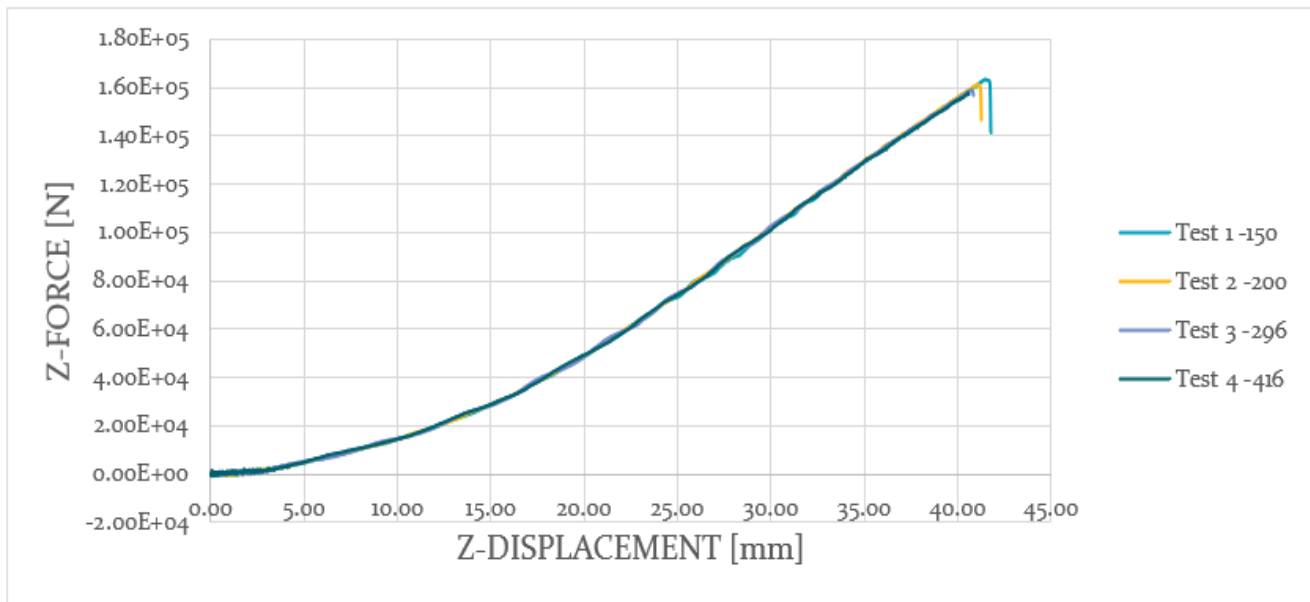


Figure 17: Force-displacement curves for four meshes.

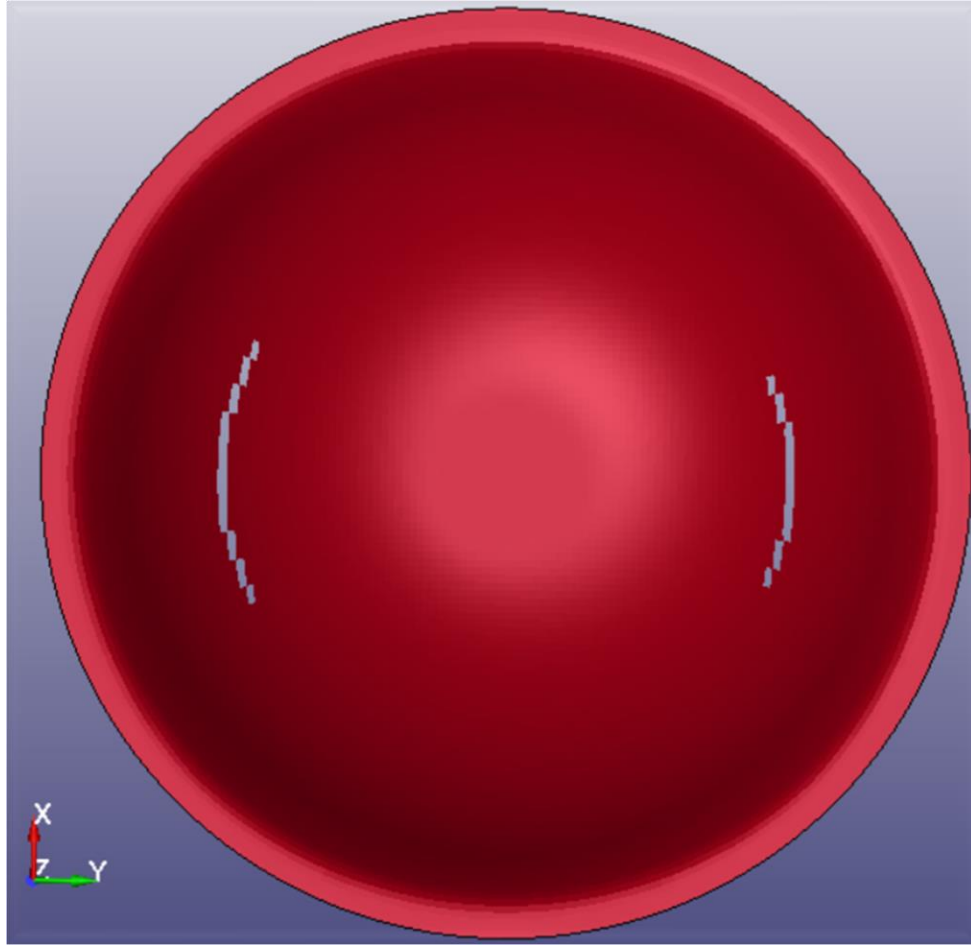


Figure 18: Fracture in the blank.

A mesh smoothing technique employed in LS-DYNA serves to refine the sharp edges within elements, giving a smoother, or more precisely, rounded contour to these sharp edges. Deployment of a mesh without smoothing techniques in LS-DYNA has resulted in a noteworthy outcome, depicted in *Figure 19* and *Figure 20*: Initially, the graph in *Figure 19* exhibits nearly identical behavior, and any slight differences can be attributed to the smoothing technique employed in LS-DYNA, which may slightly displace nodes, resulting in small variations in force-displacement. However, these variances are marginal and can be overlooked. Secondly, *Figure 20* visualizes the absence of stress concentration in the corner regions of the square, as visually indicated by a red circle within the central portion of the blank element. In subsequent analyses, a decision is made to abstain from the implementation of the smoothing technique. Minimal disparities shown in results and the absence of stress concentration within the model, will thereby enhance time efficiency.

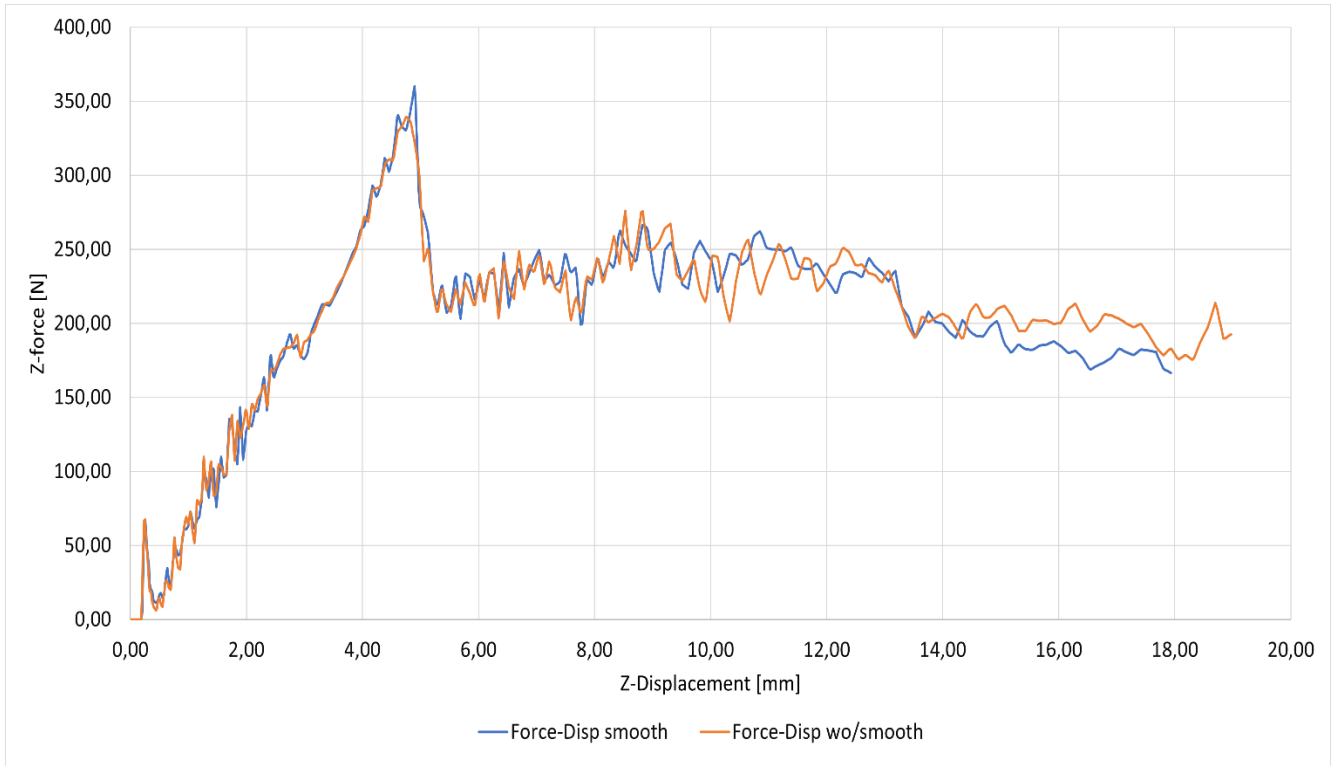


Figure 19: Force-displacement curves for the analyses with Mesh 100 with and without smoothing.

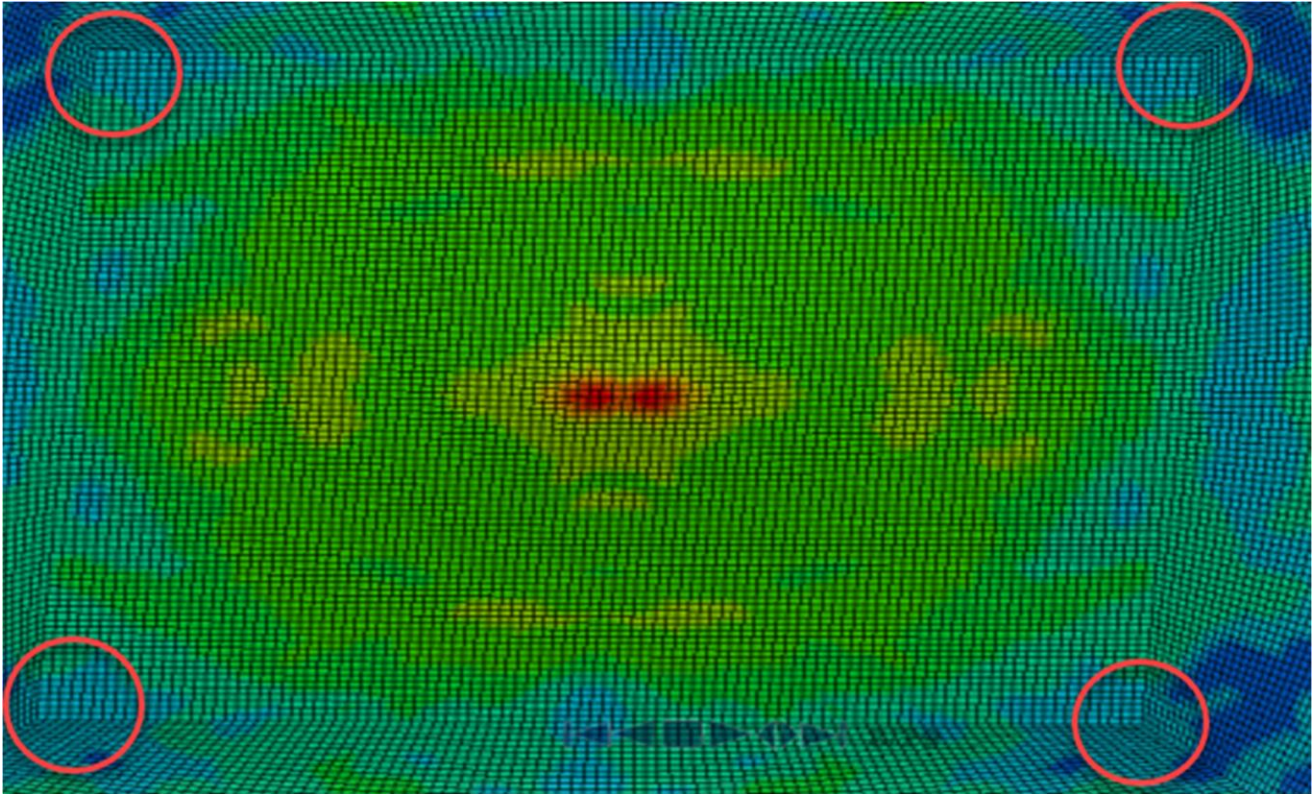


Figure 20: Mesh without smoothing.

5.3.2 Effects Of Microscopic Sheet Thickness Variations

To enhance the precision of potential Marciniak necking in the results, the variation in thickness, thickness perturbation, plays a crucial role by triggering local instabilities, which are inherent behaviors in such metals. Upon examining *Figure 21*, it becomes evident that a local necking phenomenon is occurring. The graph is limited to visualizing displacements from 25mm to 40mm, a range of interest in this investigation. This region is critical as the onset of local necking is observed around a displacement of approximately 39mm. The graph illustrates a rapid increase post-onset of necking, marked in red for clarification, ultimately leading to fracture. A small uncertainty that can contribute to determine the outcome of when the fracture occurs is the built-in thickness variation, which varies too randomly for each and every analysis one runs. The stress concentrations that occur in the grooves due to thickness variations can result, in some cases, in earlier fracture with finer meshes. An investigation into the sensitivity of force-displacement behavior was conducted, as shown in *Figure 22* and outlined in *Table 7*, by varying three distinct standard deviation coefficients, denoted in LS-DYNA as thickness perturbation coefficients, 0.004, 0.005 and 0.006mm. Specifically, LS-DYNA incorporates the specified thickness parameter of 1.51, with a considered standard deviation. The results indicates that there are relatively small variations between the three models incorporating distinct thickness variations. Further in this study, a standard deviation of 0.005 mm is employed. This parameter has been derived from a study conducted by Lademo [40].

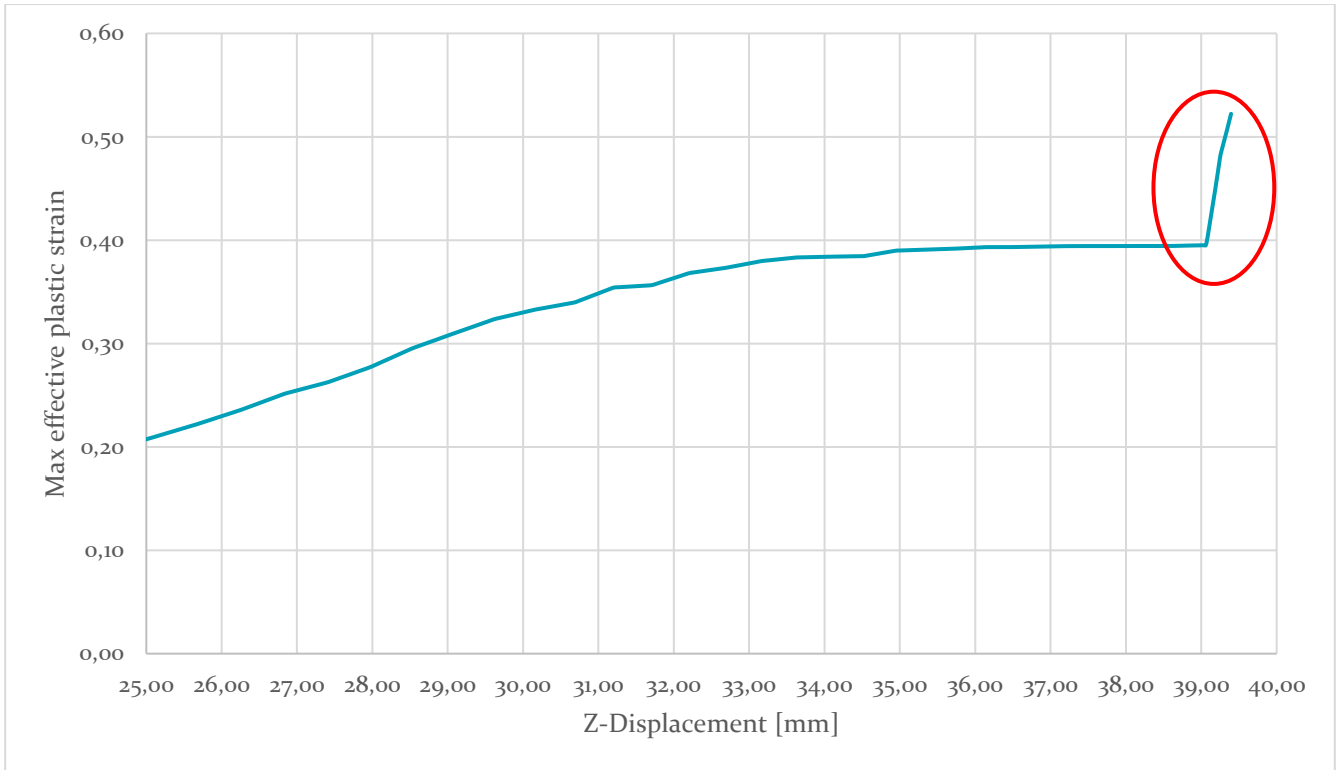


Figure 21: Local necking.

Table 7: Overview of thickness variation analyses

Shell thickness [mm]	1.51
Standard deviation input [mm]	0.004, 0.005, 0.006
Element size [mm]	1.20
Number of tests	3

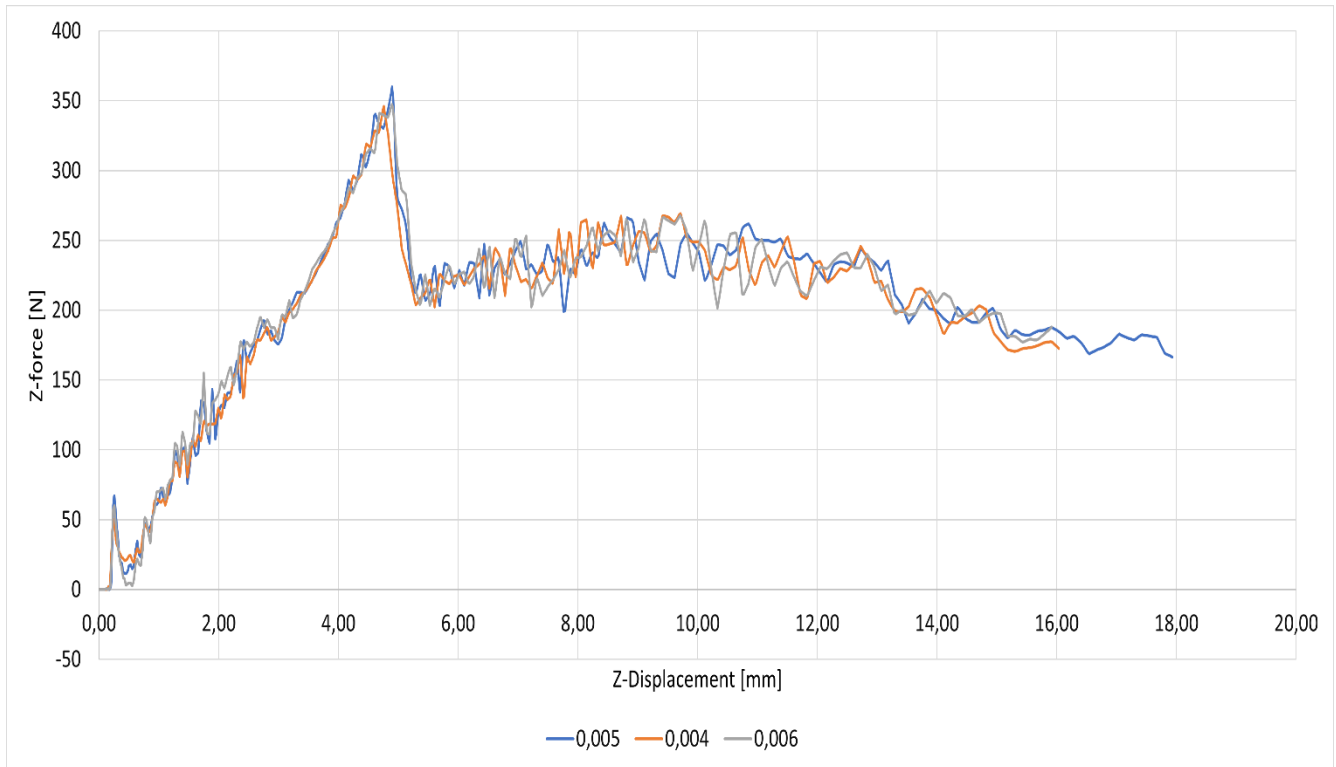


Figure 22: Force-Displacement curves from analyses with 3 distinct thickness deviation coefficients.

To identify potential unpredictable outcomes associated with the inherent stochasticity introduced by thickness variations, another parameter study is conducted. As previously noted, the thickness distribution undergoes randomization for each analysis iteration. Figure 23 presents data derived from five analogous tests outlined in Table 8, proving the identification of variations arising from the stochastic fields, introduced by the thickness perturbation.

Table 8: Overview of parameter study due to random thickness distribution

Shell thickness [mm]	1.51
Mesh density	200
Element size [mm]	1.20
Number of tests	5
Z-displacement [mm]	40.0

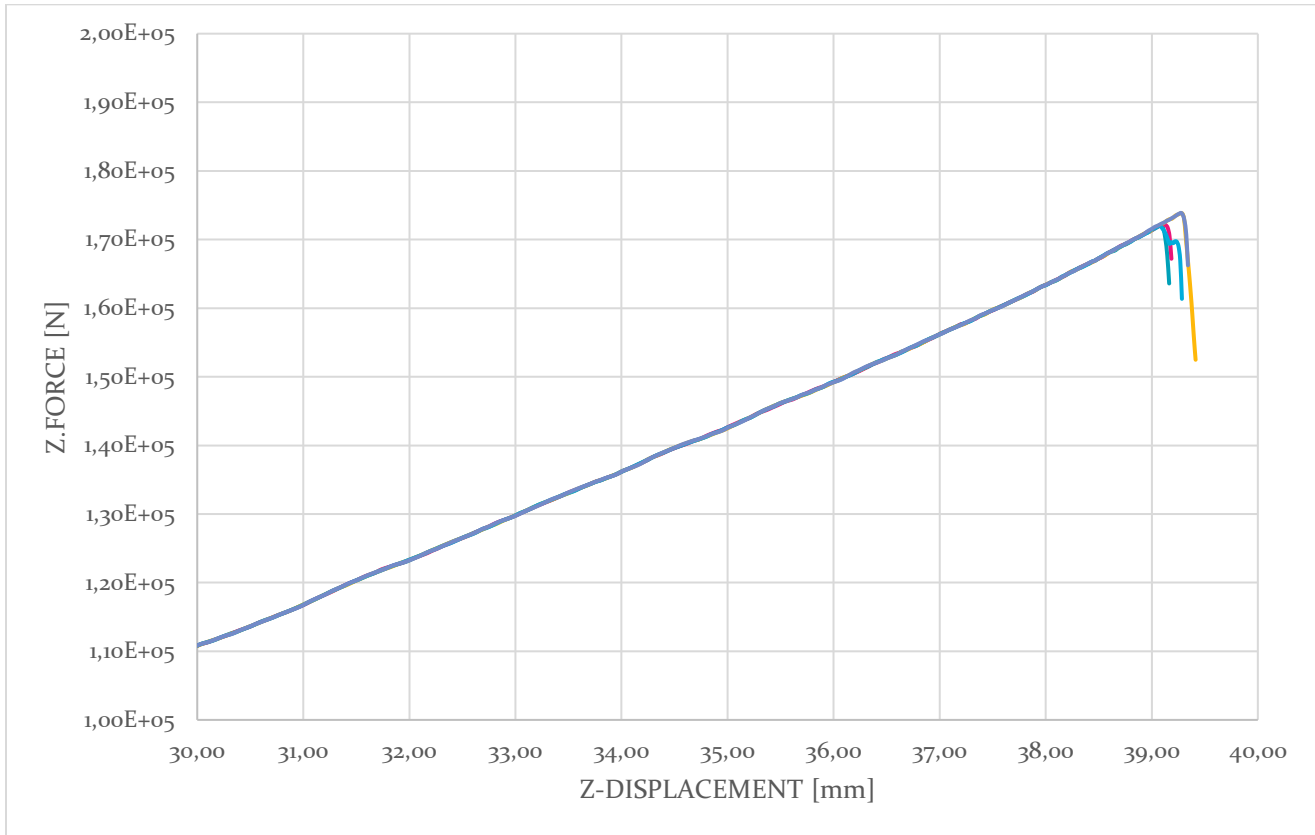


Figure 23: Force-displacement curves for five tests investigating variable outcomes.

Taking a look at *Figure 24*, the thickness variations inherent in the material is measured in pre-analyses. The terrain resembles regions similar to villages, exhibiting both elevated and low-lying regions, can also be recognized as stochastic fields. Due to this thickness variations, a hypothesis has emerged, Do these stochastic fields trigger an early failure in the deep drawing process. Due to this, a fracture in one of the analyses has been studied. The nodes/elements around the fracture zone have been the focal point of inspection and is localized before the run of the analyses and after, shown in *Figure 25*. It is evident that the fracture zone is situated where the thickness is at minimum prior to the analysis, registering 1.49 mm within the groove. The thickness reaches its maximum at 1.526 mm, with an initial thickness of 1.51 mm. It is high argued that the standard deviation of 0.005 mm is contributing to this failure. Studying the

occurrence of fractures in this sheet metal posed a significant challenge, as fractures were evidenced in distinct locations across each analysis. Fractures observed in various locations during each analysis may result from the random distribution of thickness, as depicted in *Figure 24* *Figure 25*. The fractures are consistently found within the grooves, creating an asymmetric fracture pattern. Visualizing strains that exhibits an accelerated rate of increase over short time, consequently culminating in fracture, attributed to the concentration of higher stresses in regions with reduced thicknesses. This effect arises due to the fundamental relationship between force and exposed area, where lower thicknesses result in elevated stresses. Simplifying the FEA model to investigate only one quadrant of the cup would have restricted a correctly understanding of the fracture behavior.

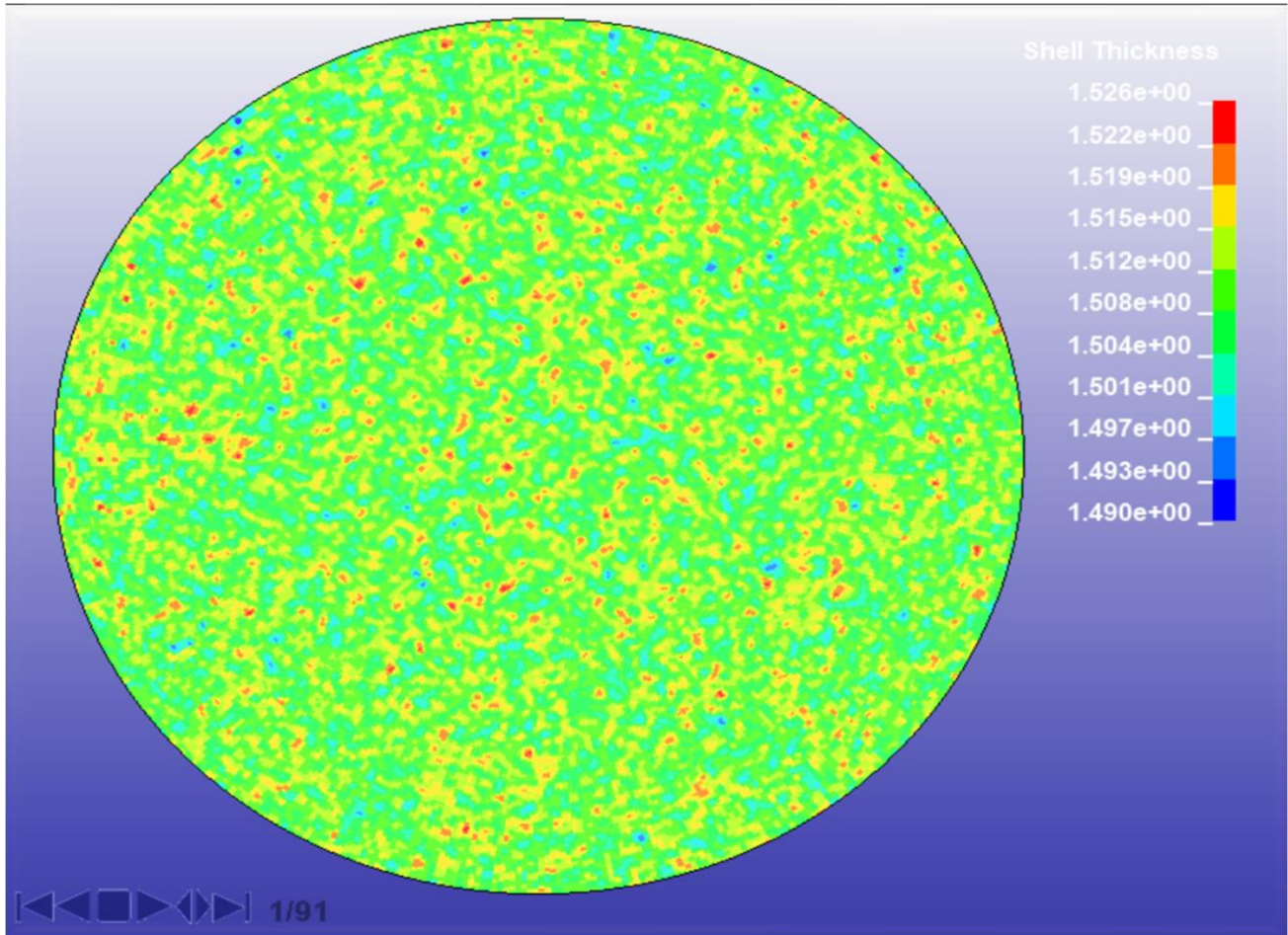


Figure 24: Thickness distribution throughout the material. Standard deviation set to 0.005 mm.

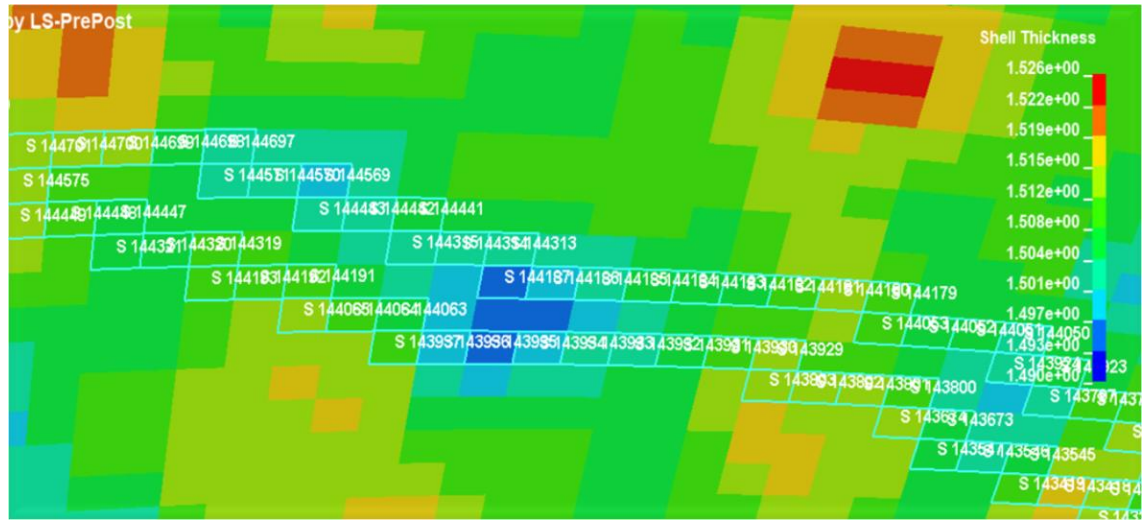


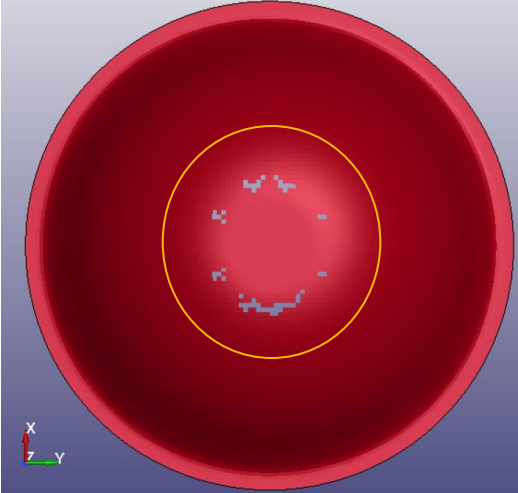
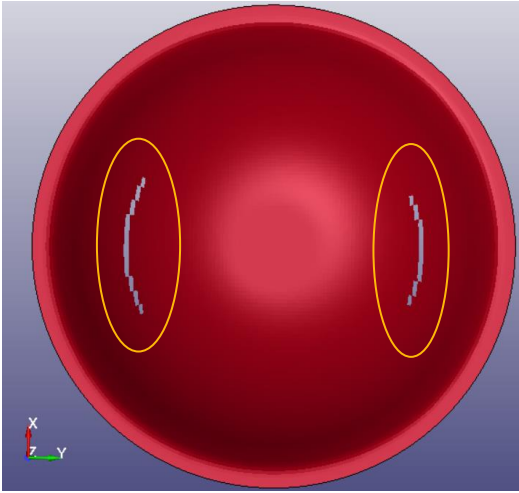
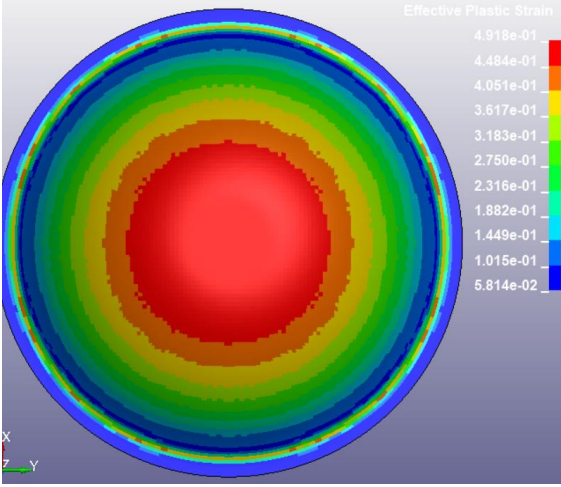
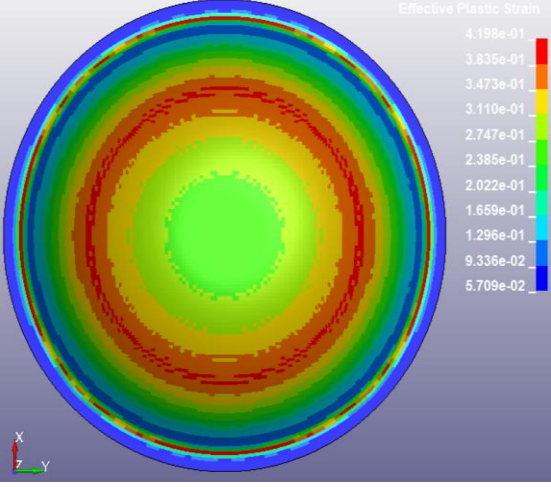
Figure 25: The location of fracture resulting from a randomly distributed shell thickness

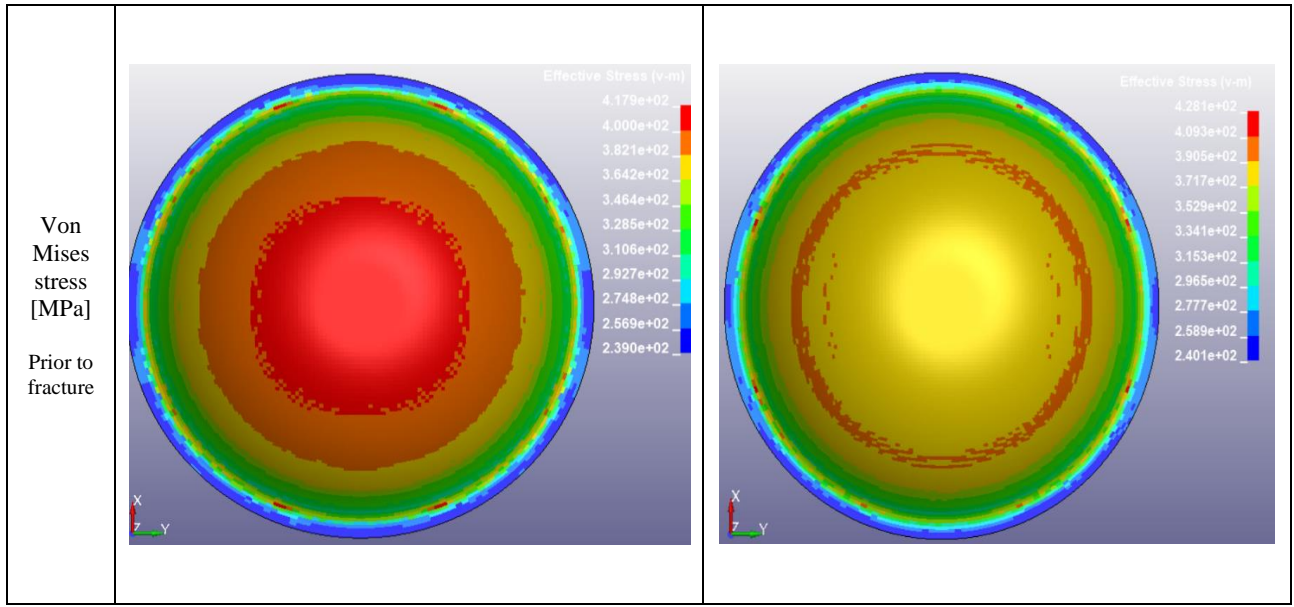
5.3.3 Effects Of Friction

Among the variables examined in the comprehensive series of analysis, one of the latest investigations focused on the friction variable. The results reveal a remarkable influence of the friction parameter on the location of fractures in the deformed blank sheet, as evidenced in *Table 9*. The inherent friction between the blank sheet and the rigid forming tools during motion can potentially serve as the origin of fracture. In contrast, the model without friction exhibited fracture at the bottom of the cup. The noted occurrence of damage at a heightened position within the cup, occurring earlier than in the frictionless scenario, can be elucidated by an increase in normal pressure between the die and the blank. This consequently results in an elevation of effective stress, resulting in highly concentrated stresses [33]. Further, the friction parameters employed in this study, static friction of 0.06 and dynamic friction of 0.03, were chosen without scientific validation. As indicated by Kothapalli in *Ch. 3.2.3*, the coefficient of friction significantly influences damage, revealing a notable increase in draw depth as the friction parameter decreases. However, an analysis conducted for a cup with a depth of 38.5mm and a blank sheet radius of 85mm, resulted in fractures with these specified friction parameters, aligning with experimental tests conducted by Sunlit Sea, serving as a validation, indicating the applicability of these friction parameters.

The reduction of thinning-induced stress concentrations in localized regions of the blank, and the improved distribution of stresses finely distributed across the blank sheet, is evident in the comparative analysis presented in *Table 9*. The table represents two distinct tests: the initial test conducted without friction parameters and the subsequent test incorporating friction parameters. The table includes damage localizations, strain plots prior to fracture, and stress plots prior to fracture respectively. In the scenario where friction parameters are not introduced, the Von Mises stresses of 418 MPa exhibit a finely distributed pattern within the bottom of the cup, as evident from the plot. In contrast, the model incorporating friction parameters, localized stresses are observed at 428 MPa prior to fracture, while stresses outside this specific region and within the bottom of the cup are denoted as 371 MPa.

Table 9: FEA results investigating friction parameter

Plot	Frictionless scenario	Static friction = 0.06 and Dynamic friction = 0.03
Fracture	 <p>A circular cross-section of a vessel with a central hole. A yellow circle highlights the central hole. Inside the hole, there are several small, irregular white and blue shapes representing fracture patterns. A 3D coordinate system (X, Y, Z) is shown in the bottom left corner.</p>	 <p>A circular cross-section of a vessel with a central hole. Two yellow ovals highlight the inner surface of the hole, one on the left and one on the right. Inside these ovals, there are white and blue shapes representing fracture patterns. A 3D coordinate system (X, Y, Z) is shown in the bottom left corner.</p>
Effective plastic Strain [-] Prior to fracture	 <p>A circular cross-section showing the distribution of effective plastic strain. The strain is highest at the center (red) and decreases towards the outer edge (blue). A color scale legend on the right indicates strain values from 5.814e-02 to 4.918e-01. A 3D coordinate system (X, Y, Z) is shown in the bottom left corner.</p>	 <p>A circular cross-section showing the distribution of effective plastic strain. The strain is highest at the center (red) and decreases towards the outer edge (blue). A color scale legend on the right indicates strain values from 5.709e-02 to 4.198e-01. A 3D coordinate system (X, Y, Z) is shown in the bottom left corner.</p>



5.2.2 Result Matrix

A set of analyses, shown in *Table 10*, has been conducted by varying two factors: the draw bead distance from the edge and cup depth, illustrated in *Figure 10* and *Figure 12*. This aims to portray a forming region wherein the cup undergoes safe deformation. The outlined forming region presented in the graph in *Figure 26* builds upon the sequence of analyses. It is evident that the draw bead distance from edge stands out as a crucial factor influencing cup depth in the drawing process as shown in *Figure 26*. By simply the draw bead distance, a significant influence is demonstrated by the quantity of material drawn into the cup, resulting in deeper cups. An argument has emerged proposing that the die shoulder radius, may impact the forming process. The die shoulder radius may have an influence on the early occurrence of fracture along the sides of the cup, consequently leading to lengthening [35]. The occurrence of wrinkling remains unobservable, potentially attributable to the selected radius of the tools [27]. Fractures were absent in the die shoulder zone, particularly during the transition from a horizontally oriented sheet to a vertically configured cup form. A small radius in the die shoulder zone could result in splitting/fracture at that place. The absence of fractures in the die shoulder zone can be associated to the compatibility of the radius in the bending zone.

Examining the graph in *Figure 26* allows a closer investigation of the behavior observed when the draw bead distance from the edge is increased by only 5mm. Notably, an elevation in draw depth by 0.5mm is discerned. This phenomenon can be attributed to the increased availability of material for cup formation, resulting in a reduction in blank elongation and consequently a deeper cup. The observed behavior remains consistent until a draw bead distance of 3mm from the edge is reached. Beyond this point, a gradual increase is observed reaching a cup depth of 41mm when the distance from the edge is increased to 20mm. In the range of 20mm to 40mm draw bead distance from the edge, the behavior remains constant, resulting in a cup depth of 41mm. A limit point of 20 mm distance from edge is evident in *Figure 26*, indicating that cup depth is no longer dependent on the distance from the edge. At this point on the graph, where the cup depth remains constant, other factors can come be considered, such as the thickness of the blank sheet. The 1.51mm thickness, coupled with an inhomogeneous thickness distribution, presents a deformation limit. Considering this, a potential increase in thickness, given its attributed benefits discussed earlier in this study, can be considered. Additionally, factors like the friction parameter can influence the shape of the convergence graph, possibly increasing the draw depth. Previous studies presented in this research emphasize the significant role of the friction parameter in deep drawing

processes. Analyses conducted in the later stages of this study reveal that a frictionless model can achieve a remarkable draw depth of 48mm.

Examining Figure 27, 28 and 29 reveals plots illustrating the Von Mises stress, effective plastic strain, and blank/shell thickness, respectively. These variables are studied throughout the forming process, providing insights into the behavior of the material. Notably, the introduction of thickness variations within the blank sheet prior to analysis creates distinct patterns resembling a net in the first quarter of the process, evident in the Von Mises plots at time 0.09. This suggests a clear influence of inherent thickness variations on the applied stresses. In the second half of the analysis, thickness distribution concentrates in different visualized fields. Even though not apparent, the inherent thickness variations continue even after the second half, as they become too small to be observable under the applied deformation. Focusing on the rim of the blank sheet, the thickness concentrates around 1.46 mm, while beyond the die shoulder radius, specifically on the side of the deformed cup, it measures 1.13 mm at the end of the analysis. This can indicate a restriction in the amount of material drawn into the cup, particularly after the die shoulder radius. Stress concentrations in a local zone following the die shoulder, as seen in the Von Mises plots, support this observation. Additionally, strain localizations near the die shoulder, where high stresses induce strain concentrations, further contribute to manifesting this observation.

Table 10: Simulation matrix

		Draw bead distance from edge [mm]									
		0.00	1.00	2.00	3.00	4.00	5.0	10.0	20.0	30.0	40.0
Depth of fracture [mm]	38.0										
	38.5										
	39.0										
	39.5										
	39.58										
	39.59										
	39.6										
	39.7										
	39.8										
	39.9										
	40.0										
	40.3										
	40.5										
	41.0										
	41.5										
	42.0										
42.5											

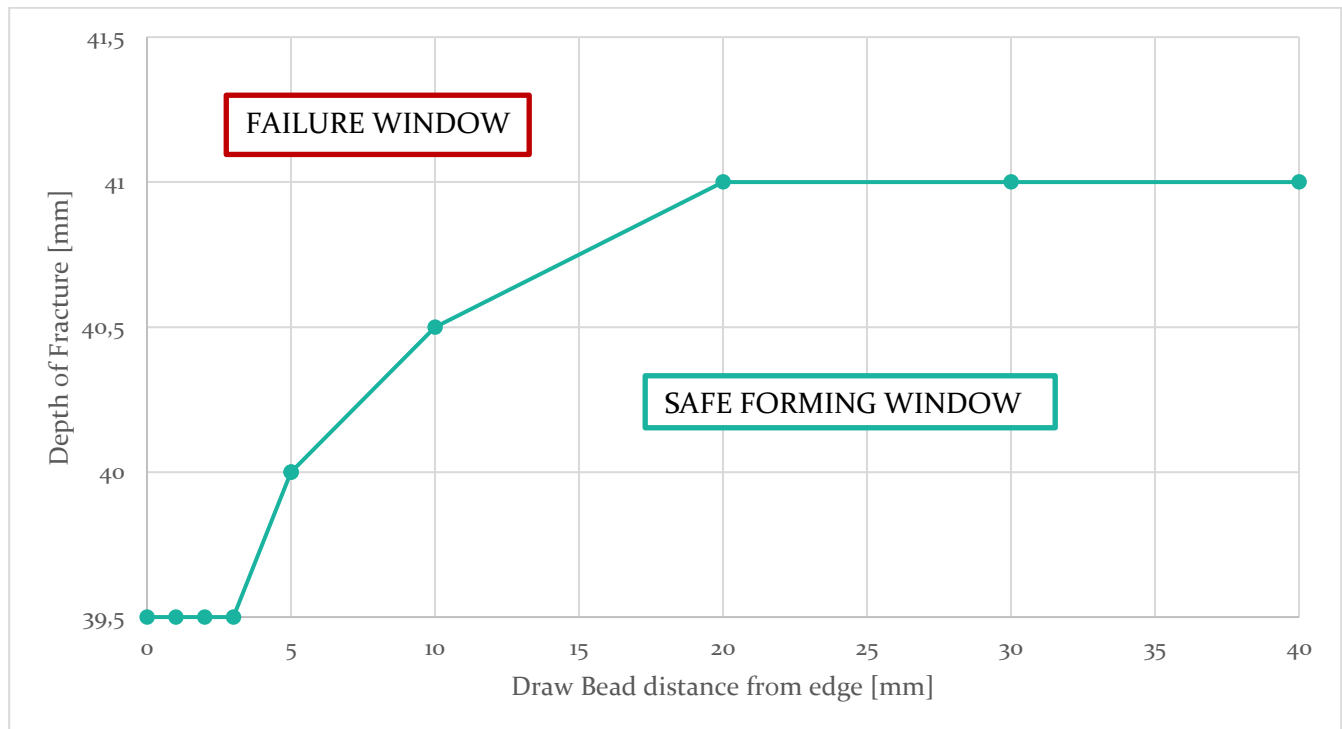
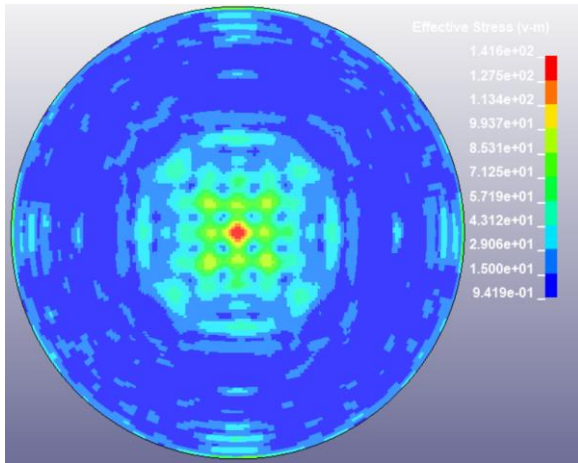
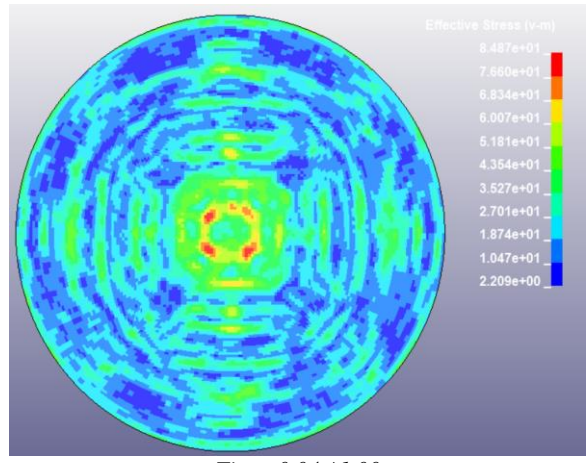


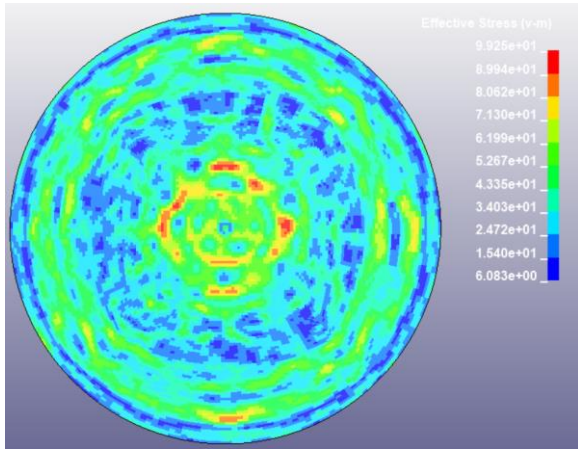
Figure 26: Region of cup forming and potential failure.



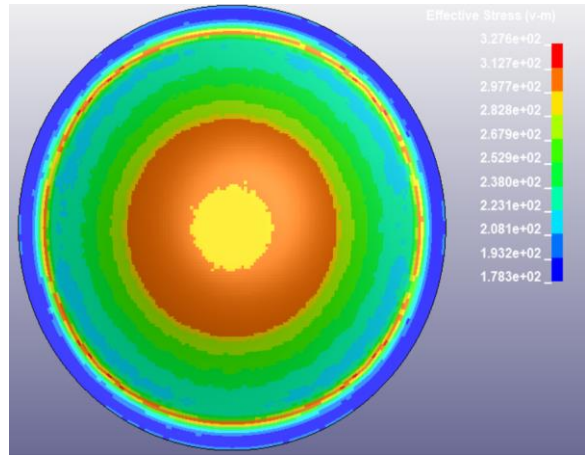
Time: 0.01 / 1.00



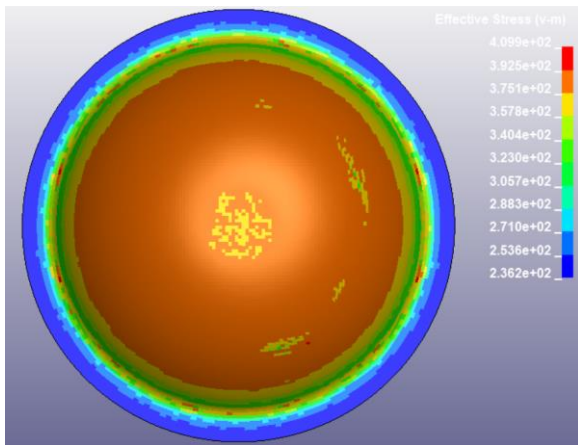
Time: 0.04 / 1.00



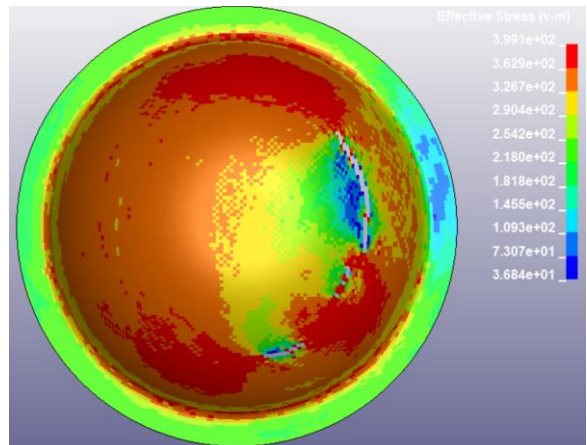
Time: 0.09 / 1.00



Time: 0.50 / 1.00

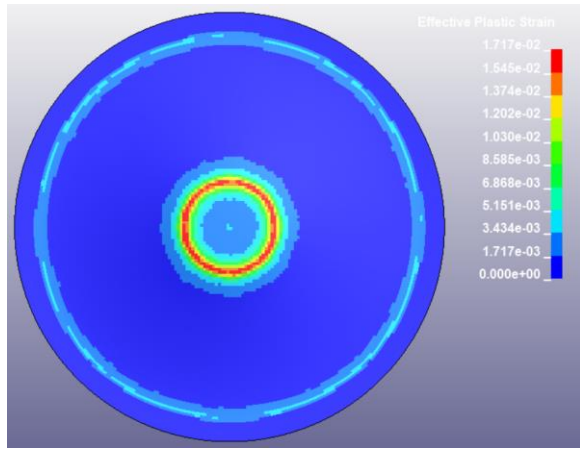


Time: 0.90 / 1.00

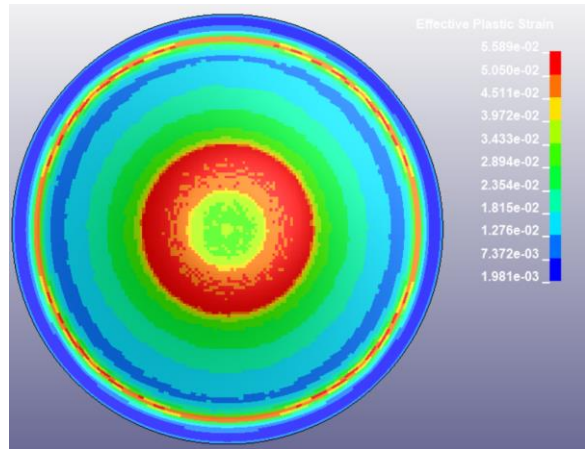


Time: 0.95 / 1.00

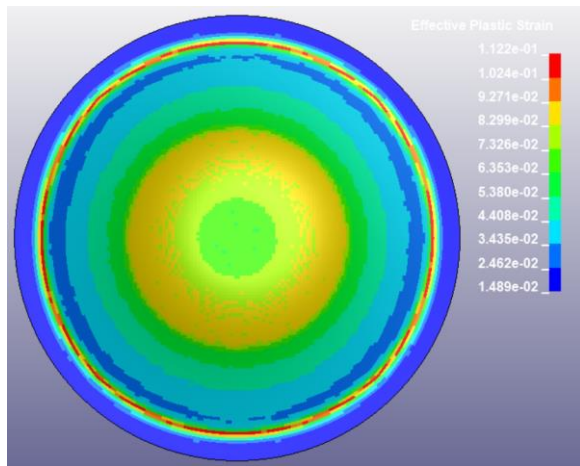
Figure 27: Von Mises stress [MPa].



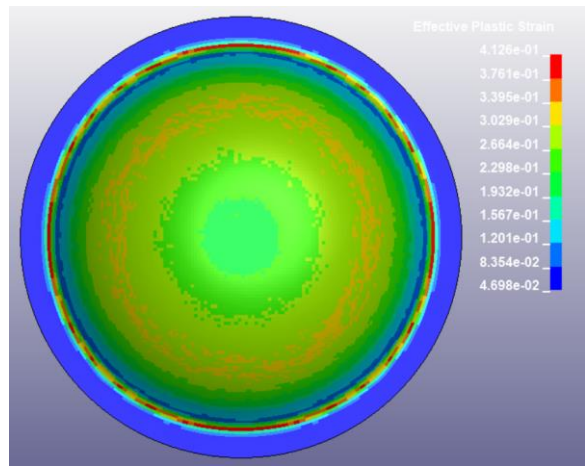
Time: 0.20 / 1.00



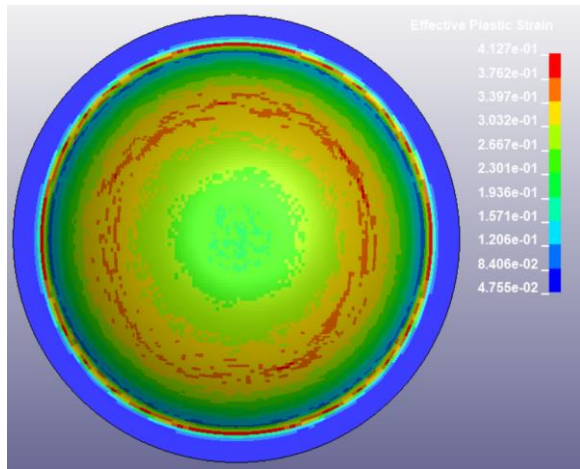
Time: 0.40 / 1.00



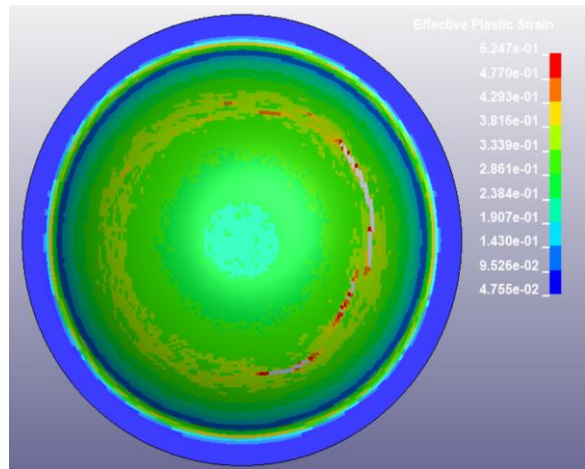
Time: 0.50 / 1.00



Time: 0.86 / 1.00

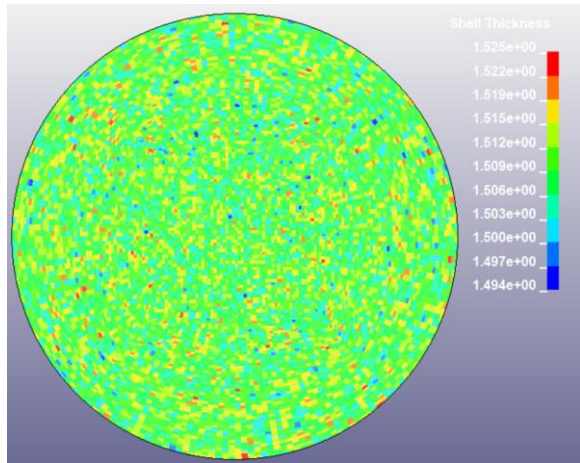


Time: 0.90 / 1.00

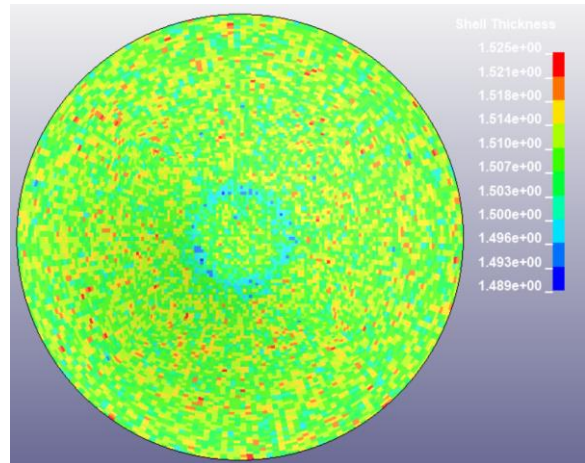


Time: 0.95 / 1.00

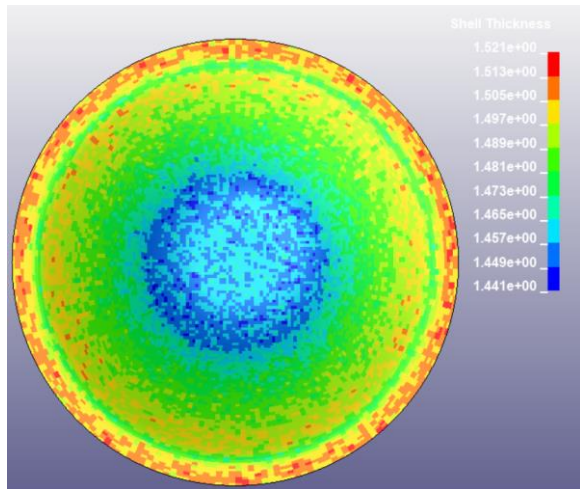
Figure 28 Effective Plastic Strain [-].



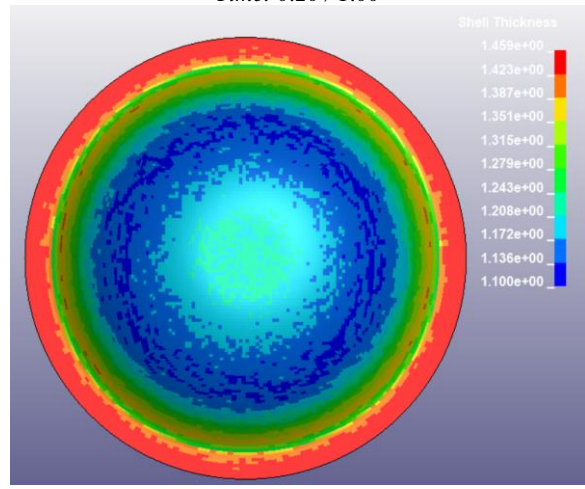
Time: 0.00 / 1.00



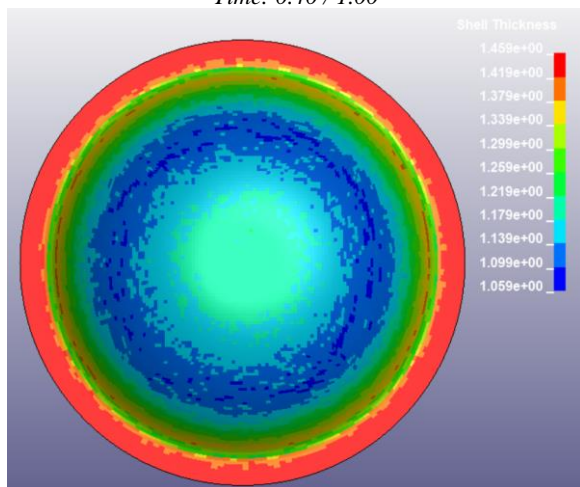
Time: 0.20 / 1.00



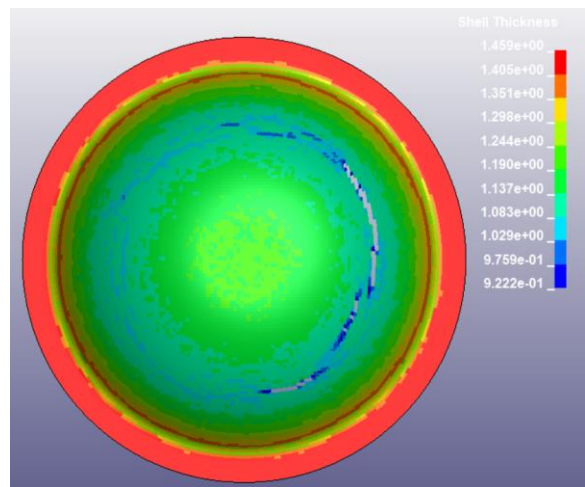
Time: 0.40 / 1.00



Time: 0.86 / 1.00



Time: 0.90 / 1.00



Time: 0.95 / 1.00

Figure 29: Shell / Blank Thickness [mm].

6 Summary and Concluding Remarks

In this investigation, a formability study is undertaken on the aluminum alloy AA5083-H111. The primary objective is to enhance the forming process of floating photovoltaic structures developed by Sunlit Sea. The study aimed to identify variables that impose limitations on the forming process and seeks ways to enhance efficiency, considering crucial factors such as time, environmental impacts, and cost-effectiveness.

The study explored the aluminum sheets, with a specific focus on the chosen aluminum sheet AA5083-H111 and its inherent anisotropic behavior. Following a thorough examination, a plasticity theory was introduced to establish a suitable framework for modelling the material behavior of this anisotropic material. The foundational theory firstly presented various yield criteria, eventually resulting in the introduction of the anisotropic yield criterion Yld2003 by Aretz [17]. This criterion, coupled with the associated flow rule, and isotropic two-term Voce hardening, precisely calibrated using a solver feature in Excel. The calibration excellently reconstructed experimental data obtained from preliminary work. Additionally, to account for inherent anisotropy developed during the manufacturing process, a random thickness variation is implemented, introducing stochastic fields, unsystematically distributed within the metal sheet. The outcome from these collaborative efforts formed the groundwork for the parameter study. Firstly, the behavior of the aluminum alloy was simulated in the FEA program, ensuring the material response aligns with expectations and identifying potential sources of error. Secondly, a set of analyses were conducted to investigate the impact of draw bead distance from the edge on the draw depth of the cup, while exploring potential physical and numerical parameters influencing this relationship.

Given that mesh dependency associated with element failure requires the incorporation of a non-local formulation, wherein failure/damage variables of neighboring elements are averaged, an examination of mesh dependency was conducted. The results conclude that a local criterion is sufficient. Varied mesh densities across different models demonstrated minimal mesh dependency, with closely similar results observed. A mesh density of 200 offers the advantage of reduced computational complexity and time efficiency.

Modeling thickness variations due to Marciniak localization is essential for capturing strain concentration in localized regions during forming. Incorporating these variations captures failure modes like necking

or fracture and provides a more accurate representation of the material during forming. These thickness variations trigger local instabilities inherent in such metals. The influence of thickness variations was clear. With a chosen standard deviation of 0.005 [40], a local necking is observed in the parameter study, where the graph showed a rapidly increasing in effective plastic strain post-onset of necking resulting in fracture immediately. It became evident that when testing a geometry close to the fracture limit, the random thickness variations can yield unpredictable results, leading to a successful forming in one analysis and fracture in another. A recommended approach involves introducing a safety margin, typically ranging from 10% to 20%, aligning with the suggestion of Keeler and Goodwin [21] [22], who introduced a safety margin by offsetting the forming limit curve in the forming limit diagram. Further investigation into the effects of microscopic sheet thickness variations has revealed fractures occurring within the grooves in the introduced stochastic fields. However, it can be concluded that strain concentrations, causing thinning, occur within the groove prior to fracture due to the implemented thickness variations.

Friction is introduced in FEA to simulate real-world conditions in metal forming processes accurately. Friction significantly influences the localization of fractures. The friction between the blank sheet and the rigid forming tools during motion can potentially serve as the origin of fracture. In contrast, the model without friction exhibited fracture at the bottom of the cup. It can be concluded that the friction results in thinning in a particular region on the side of the cup. This is due to stress localization resulting in localized strain concentrations.

Two variables were examined in correlation: the draw depth in the Z-direction and the draw bead distance from the cup's edge. The results obtained were favorable and gave an insight into the main factors affecting the successful drawing of cups. This investigation aimed to test the hypothesis that an increase in the width hold of the blank element could lead to increased material availability for deep drawing, thereby facilitating the formation of deeper cups. This positioning ranged from zero, where the blank's edge aligns with the die and punch edges, to a broader placement beyond these components. The outcomes from the analyses are presented in *Table 10* in the simulation matrix and graphically depicted in *Figure 26*, showing the region of cup forming that outlines a boundary between a safe forming window and a failure window. From the findings, it can be concluded that the draw bead distance from the edge significantly influences cup depth within a specific range of 3 mm to 20 mm. Below 3 mm, the cup depth remains constant, while at 20 mm, the forming graph converges at a depth of 41 mm. Despite the impact

of this variable, it is noteworthy that stress localizations occur around the die shoulder radius region. This result shows a constant thickness around the blank's rim after a specific point in the analysis, as the material's availability for cup formation is somewhat constrained by this region at a specific time in the forming process.

Further work

At the project's initial phase, the objective was to create a parametric design program. A tool intended to simplify the input of desired panel geometry using specified parameters. A desired functionality capable of evaluating whether a given panel could be successfully formed or result in fracture. Due to various factors, including time constraints, the project did not progress to the development of this program.

Creating such a parametric design tool would require an extensive parameter study to cover the behavior of relevant variables. A recommended path for future research involves investigating the behavior of cups with an elliptical shape, building upon the knowledge gained from this parameter study.

7 References

- [1] NASA, “What is the greenhouse effect?,” GLOBAL CLIMATE CHANGE. Accessed: Dec. 02, 2023. [Online]. Available: <https://climate.nasa.gov/faq/19/what-is-the-greenhouse-effect/>
- [2] European Commission, “Consequences of climate change,” Climate Action. Accessed: Nov. 16, 2023. [Online]. Available: https://climate.ec.europa.eu/climate-change/consequences-climate-change_en
- [3] Kloeckner Metals, “WHAT ARE THE MAJOR PROPERTIES OF ALUMINUM?,” Aluminum. Accessed: Nov. 15, 2023. [Online]. Available: <https://www.nationalgrid.com/stories/energy-explained/what-are-different-types-renewable-energy>
- [4] G. Silva and D. Branco, “Is floating photovoltaic better than conventional photovoltaic? Assessing environmental impacts,” *Impact Assessment and Project Appraisal*, vol. 36, no. 5, pp. 390–400, 2018.
- [5] Y. Choi, “A study on power generation analysis of floating PV system considering environmental impact.,” *Int J Electr Comput Energ Electron Commun Eng*, vol. 8, pp. 828–832, 2014.
- [6] ALUTRADE, “Is aluminium better for the environment than plastic,” Aluminum recycling. Accessed: Nov. 14, 2023. [Online]. Available: <https://alutrade.co.uk/is-aluminium-better-for-the-environment-than-plastic/>
- [7] S. Tveit and A. Reyes, “Experimental characterization of anisotropic plasticity in rolled AA5083-H111 sheets,” 2023.
- [8] (LSTC), “LS-DYNA® KEYWORD USER’S MANUAL VOLUME II Material Models.”
- [9] Hydro, “Here are the best aluminium alloys for bending.” Accessed: Dec. 01, 2023. [Online]. Available: <https://www.shapesbyhydro.com/en/material-properties/here-are-the-best-aluminium-alloys-for-bending/>
- [10] F. Irgens, *Continuum Mechanics*. Springer Science & Business Media, 2008.
- [11] T. Gerya, Ed., “Stress and strain,” in *Introduction to Numerical Geodynamic Modelling*, 2nd ed., Cambridge: Cambridge University Press, 2019, pp. 50–59.
- [12] Dyna Support, “From engineering to true strain, true stress,” Welcome to the LS-DYNA support site. Accessed: Dec. 03, 2023. [Online]. Available: <https://www.dynasupport.com/howtos/material/from-engineering-to-true-strain-true-stress>

- [13] R. v. Mises, “Mechanik der festen Körper im plastisch-deformablen Zustand,” *Nachrichten von der Gesellschaft der Wissenschaften zu Göttingen, Mathematisch-Physikalische Klasse*, pp. 582–592, 1913.
- [14] W. F. Hosford, “A Generalized Isotropic Yield Criterion,” *Journal of Applied Mechanics*, vol. 39, no. 2, p. 607, 1972.
- [15] R. W. Logan and W. F. Hosford, “Upper-bound anisotropic yield locus calculations assuming - pencil glide,” 1980.
- [16] F. Barlat *et al.*, “Plane stress yield function for aluminum alloy sheets—part 1: theory,” *International Journal of Plasticity*, vol. 19, no. 9, pp. 1297–1319, Sep. 2003.
- [17] H. Aretz, “A non-quadratic plane stress yield function for orthotropic sheet metals,” *Journal of Materials Processing Technology*, vol. 168, no. 1, pp. 1–9, 2005.
- [18] W. F. Langford, S. C. Snyder and J. Bausch, “New criteria for predicting the press performance of deep drawing steels,” *Trans, Amer. Soc. Metals*, vol. 42, pp. 1197–1232, 1950.
- [19] S. Tveit, “Formability analysis of AA6016-T4 aluminium alloy sheets subjected to roping,” Oslo Metropolitan University. Department of Civil Engineering and Energy Technology, 2020.
- [20] S. K. Paul, “Theoretical analysis of strain- and stress-based forming limit diagrams,” *The Journal of Strain Analysis for Engineering Design*, vol. 48, no. 3, pp. 177–188, Apr. 2013.
- [21] S. K. Paul, “Controlling factors of forming limit curve: A review,” *Advances in Industrial and Manufacturing Engineering*, vol. 2, p. 100033, May 2021.
- [22] K. Drotleff and M. Liewald, “Application of an advanced necking criterion for nonlinear strain paths to a complex sheet metal forming component,” presented at the IOP Conference Series: Materials Science and Engineering, 2018, p. 9.
- [23] Z. Marciniak, J. L. Duncan, and S. J. Hu, “Load instability and tearing (5),” in *Mechanics of Sheet Metal Forming (Second Edition)*, Z. Marciniak, J. L. Duncan, and S. J. Hu, Eds., Oxford: Butterworth-Heinemann, 2002, pp. 61–81.
- [24] R. Arrieux, “Determination and use of the forming limit stress surface of orthotropic sheets,” *Journal of Materials Processing Tech*, vol. 1 No.64, pp. 25–32, 1997.
- [25] J. P. D. M. Correia, G. Ferron, and L. P. Moreira, “Analytical and numerical investigation of wrinkling for deep-drawn anisotropic metal sheets,” *International Journal of Mechanical Sciences*, vol. 45, no. 6, pp. 1167–1180, 2003.
- [26] J. W. Hutchinson, “Plastic buckling,” *Advances in applied mechanics*, vol. 14, pp. 67–144, 1974.

- [27] D. -C. Chen, L. Cheng-Yu, and Y. Lai, "Finite element analysis of deep drawing," *Advances in Mechanical Engineering*, vol. 11, no. 9, p. 10, Sep. 2019.
- [28] Z. Marciniak, "Stability of plastic shells under tension with kinematic boundary condition," *Archiwum Mechaniki Stosowanej* 17, pp. 577–592, 1965.
- [29] H. W. Swift, "Plastic instability under plane stress," *Journal of the Mechanics and Physics of Solids*, no. 1, pp. 1–18, 1952.
- [30] A.D. Tomlenov, "Plastic stress state and stability of drawing process of complex-shaped parts," *Problems of Metal Forming Publishing house of USSR Academy of Sciences Moscow*, vol. 458, p. 14.
- [31] Z. Marciniak and K. Kuczyński, "Limit strains in the processes of stretch-forming sheet metal," *International Journal of Mechanical Sciences*, vol. 9, no. 9, pp. 609–620, Sep. 1967.
- [32] K. Chandini and A. C. Reddy, "Parametric Importance of Warm Deep Drawing Process for 1070A Aluminium Alloy: Validation through FEA," vol. 6, no. 4, 2015.
- [33] A. C. Reddy, "FORMABILITY OF SUPERPLASTIC DEEP DRAWING PROCESS WITH MOVING BLANK HOLDER FOR AA1050-H18 CONICAL CUPS," *Professor, Department of Mechanical Engineering, JNT University*, vol. 4, no. 8, pp. 124–132, 2015.
- [34] P. R. Tiwari, A. Rathore, and M. G. Bodkhe, "Factors affecting the deep drawing process – A review," *Materials Today: Proceedings*, vol. 56, pp. 2902–2908, Jan. 2022.
- [35] S. Raju, G. Ganesan, and R. Karthikeyan, "Influence of variables in deep drawing of AA 6061 sheet," *Transactions of Nonferrous Metals Society of China*, vol. 20, no. 10, pp. 1856–1862, Oct. 2010.
- [36] A. A. Reddy, "Homogenization and Parametric Consequence of Warm Deep Drawing Process for 1050A Aluminum Alloy: Validation through FEA," *International Journal of Science and Research (IJSR)*, vol. 4, pp. 2034–2042, Apr. 2015.
- [37] T. Belytschko, J. I. Lin, and C. S. Tsay, "Explicit algorithms for the nonlinear dynamics of shells," *Computer Methods in Applied Mechanics and Engineering*, vol. 42, no. 2, pp. 225–251, 1984.
- [38] (LSTC), "LS-DYNA® KEYWORD USER'S MANUAL VOLUME I," 2021.
- [39] M. Bischoff and E. Ramm, "Shear deformable shell elements for large strains and rotations," *Int. J. Numer. Methods Eng.*, vol. 40, pp. 4427–4449, 1997.
- [40] O. -G. Lademo, T. Berstad, O. S. O. Hopperstad, and K. O. Pedersen, "A numerical tool for formability analysis of aluminium alloys. Part I: Theory," *Steel Grips*, no. 2, 2004.

[41] O. -G. Lademo, T. Berstad, O. S. Hopperstad, and K. O. Pedersen, "A numerical tool for formability analysis of aluminium alloys. Part II: Experimental validation," *Steel Grips*, no. 2, 2004.